Subducted slabs stagnant above, penetrating through, and trapped below the 660 km discontinuity

Yoshio Fukao[1] and Masayuki Obayashi[2]

[1]   A new *P* wave tomographic model of the mantle was constructed using more than 10 million travel times. The finite-frequency effect of seismic rays was taken into account by calculating banana-donut kernels at 2 Hz for all first arrival time data, and at 0.1 Hz for broadband differential travel time data. Based on this model, a systematic survey for subducted slab images was developed for the circum-Pacific; including the Kurile, Honshu, Izu-Bonin, Mariana, Java, Tonga-Kermadec, southern and northern South America, and Central America, arcs. This survey revealed a progressive lateral variation of the configuration of slabs along arc(s), which we interpret as an indication for successive stages of slab subduction through the Bullen's transition region with the 660 km discontinuity at the middle. We identified the four distinct stages: I - slab stagnant above the 660 km discontinuity; II - slab penetrating the 660 km discontinuity; III - slab trapped in the uppermost lower mantle (at a depth of 660–1000 km); and IV - slab descending well into the deep lower mantle. The majority of slab images are found to be either at Stage I or III, suggesting that Stages I and III are relatively stable or neutral and II and IV are relatively unstable or transient. There is a remarkable distinction for the deepest hypocentral distribution between slabs at Stage I and slabs at Stages II or III.

Citation: Fukao, Y., and M. Obayashi (2013), Subducted slabs stagnant above, penetrating through, and trapped below the 660 km discontinuity, *J. Geophys. Res. Solid Earth*, *118*, 5920–5938, doi:10.1002/2013JB010466.

1.   Introduction

[2]   In a review of tomographic images of subducted slabs around the circum-Pacific, *Fukao et al.* [2001] revealed that subducted slabs tend to be trapped not only above the 660 km discontinuity (hereafter referred to as "the 660") but also across or below it, at depth ranges of ∼ 400–1000 km (defined by *Bullen* [1963] as being the transition region between the upper and lower mantle). Such a tendency implies that the entire depth range of Bullen's transition region (with the 660 at the middle) plays a significant role in slab subduction. *Fukao et al.* [2001] substantiated this implication by pointing out the richness of reported seismic discontinuities in the lower half of the Bullen's transition region including *Kawakatsu and Niu* [1994] (see also the review by *Kind and Li* [2007], *Courtier et al.* [2007], *Courtier \and Revenaugh* [2008], *Andrews and Deuss* [2008], and *Cao et al.* [2010]), contrasted lateral heterogeneity patterns across depths of ∼ 1000 km in some global tomographic models, and a complex viscosity structure in the uppermost lower mantle in some geodynamic models (see also *Steinberger* [2000], *Forte and Mitrovica*

[2001], *Mitrovica and Forte* [2004], and *Steinberger and Holme* [2008]). In particular, *Wen and Anderson* [1995, 1997] interpreted the uppermost lower mantle as being the bottom layer of the vigorous convection system, involving surface plate motion and slab subduction as an integral part.

[3]   More recent tomographic studies have sharpened the images of deeply subducted slabs considerably [e.g., *Zhao*, 2004; *Li et al.*, 2008; *van der Meer et al.*, 2009; *Simmons et al.*, 2012]. However, to our knowledge, none have addressed the possibly unique role of the uppermost lower mantle in the process of slab subduction. In this present paper, we attempt a systematic survey of slab images around the circum-Pacific in our tomographic model to find any systematic changes of slab configuration along arc(s). We interpret such changes as being slabs at successively different stages of subduction through the Bullen's transition region, where we identify four distinctive stages: Stage I - slab stagnation above the 660; II - slab penetration through the 660; III - slab trap in the uppermost lower mantle; and IV - slab descent into the deep lower mantle. In particular, we emphasize the stage at which a penetrated slab is trapped in the uppermost lower mantle. We also point out the remarkable distinction for the deepest hypocentral distribution between stagnant slabs in the transition zone and trapped slabs in the uppermost lower mantle.

2.   Data Sources and the Model

[4]   The slab images shown in the next section are based on our new mantle model inverted from *P* wave travel

────────────
[1]Institute for Research on Earth EvolutionJapan Agency for Marine-Earth Science and Technology, Yokohama, Kanagawa, Japan.
[2]Institute for Research on Earth Evolution, Japan Agency for Marine-Earth Science and Technology, Yokosuka, Kanagawa, Japan.

Corresponding author: Y. Fukao, Institute for Research on Earth Evolution, Japan Agency for Marine-Earth Science and Technology, Showa, Kanazawa, Yokohama, Kanagawa 236-0001, Japan. (fukao@jamstec.go.jp)
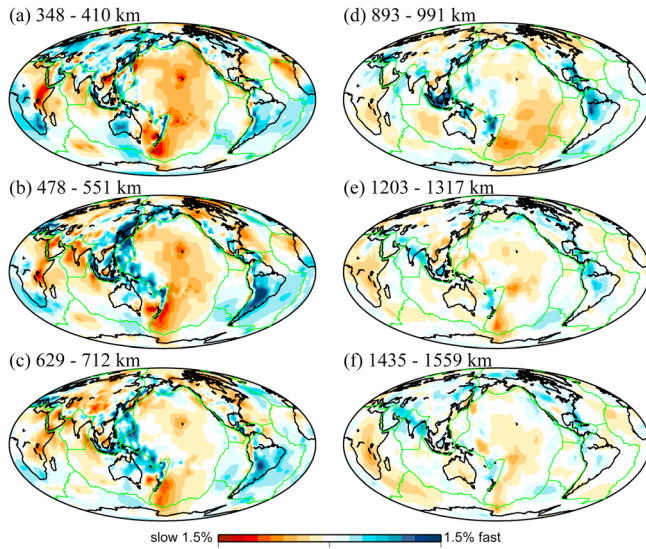
Figure 1. Velocity perturbation maps of GAP_P4: (a) just above the transition zone; (b) in the transition zone; (c) across the 660 km discontinuity; (d) in the uppermost lower mantle; (e) below the uppermost lower mantle; and (f) in the midlower mantle.

time data (see *Obayashi et al.* [2013] for details). The model is an update of GAP_P2 [*Obayashi et al.*, 2009] derived from ~7.4 million first arrival times reported to the International Seismological Center (ISC), in addition to the first arrival times of ~50,000 *P* waves manually picked from regional network records in the central to western Pacific region, and ~15,000 PP-P differential travel times obtained by a waveform correlation of P and PP waveforms from global broadband networks with a correction for time shifts due to crustal reverberations at PP bounce points [*Obayashi et al.*, 2004]. The new model GAP_P4 is different from the earlier model (GAP_P2) in two respects. First, it uses ~11.3 million first arrival time data from the ISC bulletin (1964–2008) and ~60,000 onset times visually picked from broadband

seismograms from regional networks in the western Pacific. In addition to these first arrival time data, we used the earlier set of ~15,000 PP-P differential time data, to which we added ~4300 station-to-station differential travel time data from the Broadband Ocean Bottom Seismograph arrays deployed in the northwestern Pacific [*Shiobara et al.*, 2009] and ~900 such data from the Russian Far East broadband seismic array [*Miyamachi et al.*, 2009]. The second way, in which the GAP_P4 differs from the earlier GAP_P2, is that it corrects all travel time data for the finite-frequency effect by calculating banana-doughnut kernels [*Dahlen et al.*, 2000; *Mercerat and Nolet*, 2013]. All the first arrival time data are assumed to be those at 2 Hz by referring to *Oki et al.* [2004], and all the broadband differential travel time data are assumed to be those at 0.1 Hz. Finite frequency corrections to the broadband data are proved to be very important for sharpening the slab images beneath the Mariana by *Obayashi et al.* [2013]. The new model is available from http://www.jamstec.go.jp/pacific21/google_earth/kmlgenerator/tomography.html.

3. Slab Images Around the Circum-Pacific

[5] Figure 1 shows velocity perturbation maps of (a) just above the transition zone (348–410 km); (b) in the transition zone (478–551 km); (c) across the 660 km discontinuity (629–712 km); (d) in the uppermost lower mantle (893–991 km); (e) below the uppermost lower mantle (1203–1317 km); and (f) in the midlower mantle (1435–1559 km). We can observe narrowly concentrated signals of downgoing slabs in Figure 1a; extensively broadened signals of stagnant slabs in Figure 1b; less broadened signals of penetrating slabs Figure 1c; rebroadened signals of trapped slabs below the 660 in Figure 1d; the fading of presently subducting slab signals and the emergence of remnant slab signals in the Himalayas (Tethys anomaly), and North America (Farallon anomaly) [*Grand et al.*, 1997; *van der Hilst et al.*, 1997] in Figure 1e; and persistence of this situation in Figure 1f. We note here a geographical nonoverlap between the broadened signals of stagnant slabs above the 660 in Figure 1b and rebroadened signals of trapped slabs
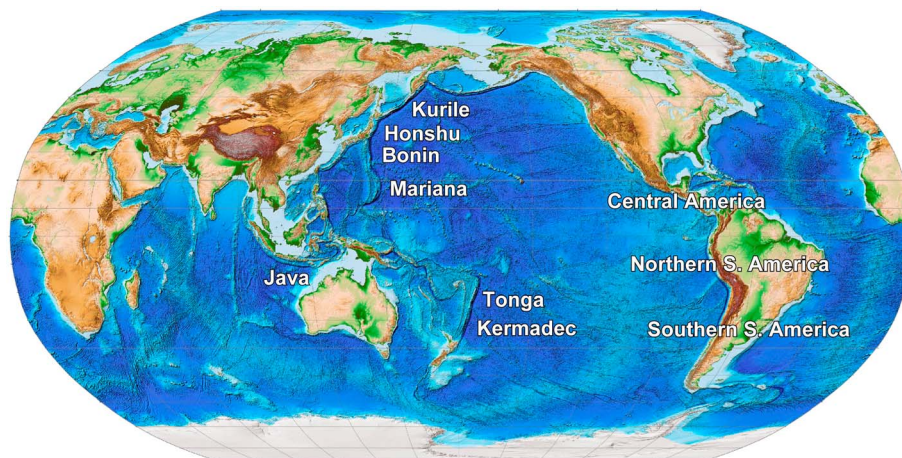

Figure 2. Survey targets for tomographic images of subducted slabs around the circum-Pacific.
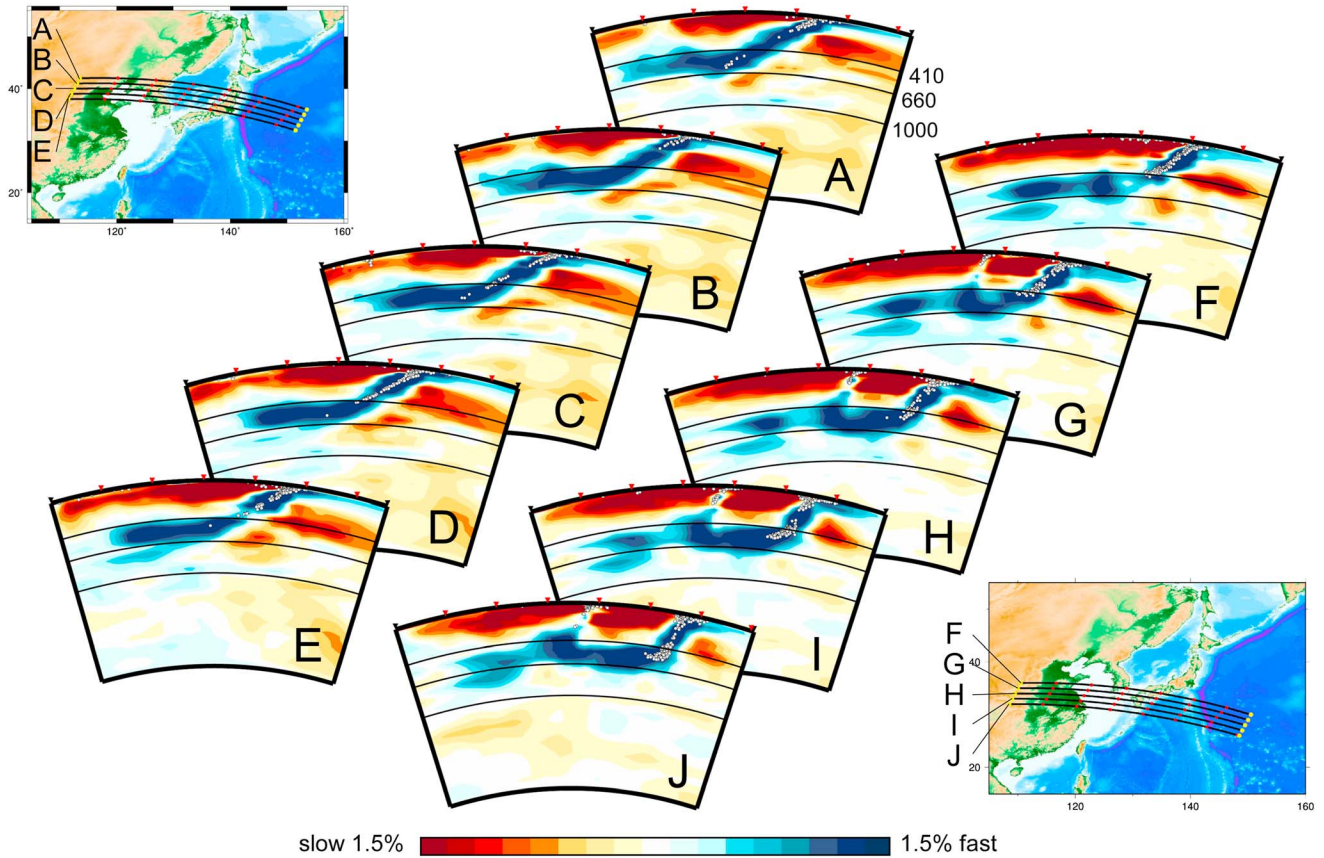
Figure 3. Successive slices of slab images. (top, left) Across the northern Honshu arc along profiles A–E shown in the top left map. (bottom, right) Across the northern Bonin arc along profiles F–J shown in the bottom right map. The color scale is ± 1.5% in *P* wave velocity perturbation (blue = positive, red = negative). White dots indicate earthquake hypocenters within a band 50 km wide on both sides of the section plane. The three depth lines indicate the top (410 km) and bottom (660 km) of the transition zone and the bottom of the uppermost lower mantle (which is rather arbitrarily placed at 1000 km depth). Tics are added on the upper frame of each cross section at every 5° from the left hand side. Their locations are shown along each profile in the two maps.

below the 660 in Figure 1d, across less broadened signals of penetrating slabs in Figure 1c.

[6] We visit typical subduction zones around the circum-Pacific, including those of (1) Honshu-Izu-Bonin-Mariana; (2) Kurile; (3) Java; (4) Tonga-Kermadec; (5) South America; and (6) Central America (Figure 2). In each of these places, the tomographic cross sections are taken along the mutually parallel, equally spaced profiles to minimize the bias that might be associated with a judicious selection of the cross sections. However, the choice of the orientation of the mutually parallel profiles for each arc is somewhat subjective. Profiles parallel to the seafloor spreading direction, and those normal to the trench, are two obvious choices, but neither choice is often considered to be the best choice for delineating slab configuration. Instead therefore, we take many mutually parallel profiles at equal intervals, roughly normal to the trench, so that consideration of the exact choice of profile orientation is not of undue importance. We also adopt a uniform velocity perturbation scale of ±1.5% for all the cross sections. Bullen's transition region is indicated by the three depth lines at 410, 660, and 1000 km. The

1000 km depth line is not a well-defined boundary but is used to give a measure of the approximate bottom of the uppermost lower mantle. Earthquake hypocenters within a band measuring 50 km wide on both sides of the section plane are also shown, based on the EHB (Engdahl-Hilst-Buland) Bulletins published from the ISC (http://www.isc.ac.uk/ehbbulletin) [*Engdahl et al.*, 1998]. The resolution of a slab image is strongly region dependent, as discussed in the Appendix A. In the following sections, we discuss the slab images that are considered to have resolvable features.

3.1. Honshu-Izu-Bonin-Mariana

[7] Figure 3 shows successive southward cross sections across the northern Honshu arc (A–E), and across the northern Bonin arc (F–J), providing typical images of stagnant slabs above the 660. Stagnant slab features in these regions have been repeatedly reported. *Fukao et al.* [2001] provides earlier references (including *van der Hilst et al.* [1991] and *Fukao et al.* [1992], and more recent references include *Miller et al.* [2004], *Huang and Zhao* [2006], *Li et al.* [2008], *van der Meer et al.* [2009], *Zhao et al.* [2009],

Table 1. Detail of the Cross Sections, Slab Images, and Deepest Earthquakes

	Honshu (Figure 3)				
	section A	section B	section C	section D	section E
End point P	113.5°E, 42.0°N	113.0°E, 41.0°N	112.5°E, 40.0°N	112.0°E, 39.0°N	111.5°E, 38.0°N
End point Q	153.5°E, 36.0°N	153.0°E, 35.0°N	152.5°E, 34.0°N	152.0°E, 33.0°N	151.5°E, 32.0°N
Interpreted stage	I	I	I	I	I
Deepest shock (km)	600	195	561	566	492
Subhorizontal deep shocks	−	−	−	−	−
	Northern Bonin (Figure 3)				
	section F	section G	section H	section I	section J
End point P	110.5°E, 36.0°N	110.0°E, 35.0°N	109.5°E, 34.0°N	109.0°E, 33.0°N	108.5°E, 32.0°N
End point Q	150.5°E, 30.0°N	150.0°E, 29.0°N	149.5°E, 28.0°N	149.0°E, 27.0°N	148.5°E, 26.0°N
Interpreted stage	I	I	I	I	I
Deepest shock (km)	432	449	505	521	541
Subhorizontal deep shocks	Yes	Yes	Yes	Yes	Yes
	Southern Bonin (Figure 4)				
	section A	section B	section C	section D	section E
End point P	116.0°E, 25.2°N	116.0°E, 24.2°N	116.0°E, 23.2°N	116.0°E, 22.2°N	116.0°E, 21.2°N
End point Q	150.0°E, 31.2°N	150.0°E, 30.2°N	150.0°E, 29.2°N	150.0°E, 28.2°N	150.0°E, 27.2°N
Interpreted stage	I	I	I	I	I
Deepest shock (km)	521	532	583	552	587
Subhorizontal deep shocks	Yes	Yes	Yes	Yes	−
	Northern Mariana (Figure 4)				
	section F	section G	section H	section I	section J
End point P	116.0°E, 20.2°N	116.0°E, 18.2°N	116.0°E, 16.2°N	116.0°E, 14.2°N	116.0°E, 12.2°N
End point Q	150.0°E, 26.2°N	150.0°E, 24.2°N	150.0°E, 22.2°N	150.0°E, 20.2°N	150.0°E, 18.2°N
Interpreted stage	I-II	I-II	I-II	I-II-III	I-II-III
Deepest shock (km)	520	644	350	502	608
Subhorizontal deep shocks	−	−	−	−	−
	Southern Kurile (Figure 6)				
	section A	section B	section C	section D	section E
End point P	123.5°E, 54.5°N	124.5°E, 55.5°N	125.5°E, 56.5°N	126.5°E, 57.5°N	127.5°E, 58.5°N
End point Q	151.5°E, 36.0°N	152.5°E, 37.0°N	153.5°E, 38.0°N	154.5°E, 39.0°N	155.5°E, 40.0°N
Interpreted stage	I	I	I-II	I-II	I-II
Deepest shock (km)	470	536	406	604	583
Subhorizontal deep shocks	−	−	−	−	−
	Northern Kurile (Figure 6)				
	section F	section G	section H	section I	section J
End point P	130.5°E, 61.5°N	131.5°E, 62.5°N	132.5°E, 63.5°N	133.5°E, 64.5°N	134.5°E, 65.5°N
End point Q	158.5°E, 43.0°N	159.5°E, 44.0°N	160.5°E, 45.0°N	161.5°E, 46.0°N	162.5°E, 47.0°N
Interpreted stage	II	II	II-III	II-III	II-III
Deepest shock (km)	681	650	634	649	446
Subhorizontal deep shocks	−	−	−	−	−
	Eastern Java (Figure 8)				
	section A	section B	section C	section D	section E
End point P	118.0°E, 15.0°S	116.0°E, 15.0°S	114.0°E, 15.0°S	112.0°E, 15.0°S	110.0°E, 15.0°S
End point Q	133.0°E, 15.0°N	131.0°E, 15.0°N	129.0°E, 15.0°N	127.0°E, 15.0°N	125.0°E, 15.0°N
Interpreted stage	I	II	II	II	II-III
Deepest shock (km)	618	641	636	679	526
Subhorizontal deep shocks	Yes	−	−	−	−
	Western Java (Figure 8)				
	section F	section G	section H	section I	section J
End point P	107.0°E, 15.0°S	106.0°E, 15.0°S	105.0°E, 15.0°S	104.0°E, 15.0°S	103.0°E, 15.0°S
End point Q	122.0°E, 15.0°N	121.0°E, 15.0°N	120.0°E, 15.0°N	119.0°E, 15.0°N	118.0°E, 15.0°N
Interpreted stage	II-III-	II-III-	II-III-	II-III-	II-III-
Deepest shock (km)	625	656	656	577	659
Subhorizontal deep shocks	−	−	−	−	−
	Tonga (Figure 10)				
	section A	section B	section C	section D	section E
End point P	160.0°E, 16.0°S	160.0°E, 17.0°S	160.0°E, 18.0°S	160.0°E, 19.0°S	160.0°E, 20.0°S
End point Q	168.0°W18.0°S	168.0°W, 19.0°S	168.0°W, 20.0°S	168.0°W, 21.0°S	168.0°W, 22.0°S
Interpreted stage	I-II-III	I-II-III	I-II-III	I-II-III-	I-II-III-
Deepest shock (km)	700	696	692	675	683
Subhorizontal deep shocks	Yes	Yes	Yes	Yes	Yes
	Kermadec (Figure 10)				
	section F	section G	section H	section I	section J
End point P	160.0°E, 22.0°S	160.0°E, 23.0°S	160.0°E, 24.0°S	160.0°E, 25.0°S	160.0°E, 26.0°S
End point Q	168.0°W, 24.0°S	168.0°W, 25.0°S	168.0°W, 26.0°S	168.0°W, 27.0°S	168.0°W, 28.0°S
Interpreted stage	II-III-	II-III-	II-III-	II-III-	II-III-
Deepest shock (km)	700	692	700	620	639
Subhorizontal deep shocks	−	−	−	−	−

Table 1. (continued)

	section A	section B	section C	section D	section E
Northern Chile (Figure 12)					
End point P	80.0°W, 19.0°S	80.0°W, 20.0°S	80.0°W, 21.0°S	80.0°W, 22.0°S	80.0°W, 23.0°S
End point Q	50.0°W, 19.0°S	50.0°W, 20.0°S	50.0°W, 21.0°S	50.0°W, 22.0°S	50.0°W, 23.0°S
Interpreted stage	I	I	I	I	I
Deepest shock (km)	593	576	550	580	580
Subhorizontal deep shocks	–	–	–	Yes	Yes
Southern Chile (Figure 12)					
	section F	section G	section H	section I	section J
End point P	80.0°W, 24.0°S	80.0°W, 26.0°S	80.0°W, 28.0°S	80.0°W, 30.0°S	80.0°W, 32.0°S
End point Q	50.0°W, 24.0°S	50.0°W, 26.0°S	50.0°W, 28.0°S	50.0°W, 30.0°S	50.0°W, 32.0°S
Interpreted stage	I	I	I	I	I
Deepest shock (km)	577	611	610	195	161
Subhorizontal deep shocks	–	–	–	–	–
Southern Peru (Figure 13)					
	section A	section B	section C	section D	section E
End point P	80.0°W, 17.0°S	80.0°W, 16.0°S	80.0°W, 15.0°S	80.0°W, 14.0°S	80.0°W, 13.0°S
End point Q	50.0°W, 17.0°S	50.0°W, 16.0°S	50.0°W, 15.0°S	50.0°W, 14.0°S	50.0°W, 13.0°S
Interpreted stage	I-II	I-II	I-II	II-III	II-III
Deepest shock (km)	611	591	592	640	640
Subhorizontal deep shocks	–	–	–	–	–
Northern Peru (Figure 13)					
	section F	section G	section H	section I	section J
End point P	80.0°W, 12.0°S	80.0°W, 11.0°S	80.0°W, 10.0°S	80.0°W, 9.0°S	80.0°W, 8.0°S
End point Q	50.0°W, 12.0°S	50.0°W, 11.0°S	50.0°W, 10.0°S	50.0°W, 9.0°S	50.0°W, 8.0°S
Interpreted stage	II-III-	II-III-	II-III-	II-III-	II-III-
Deepest shock (km)	114	623	634	622	656
Subhorizontal deep shocks	–	–	–	–	–
Northern Central America (Figure 16)					
	section A	section B	section C	section D	section E
End point P	99.5°W, 15.0°N	98.5°W, 14.0°N	97.5°W, 13.0°N	96.5°W, 12.0°N	95.5°W, 11.0°N
End point Q	77.0°W, 38.15°N	76.0°W, 37.15°N	75.0°W, 36.15°N	74.0°W, 35.15°N	73.0°W, 34.15°N
Interpreted stage	I-II-III	I-II-III	II-III-	II-III-	II-III-IV
Deepest shock (km)	68	112	191	241	256
Subhorizontal deep shocks	–	–	–	–	–
Middle Central America (Figure 16)					
	section F	section G	section H	section I	section J
End point P	94.5°W, 10.0°N	93.5°W, 9.0°N	92.5°W, 8.0°N	91.5°W, 7.0°N	90.5°W, 6.0°N
End point Q	72.0°W, 33.15°N	71.0°W, 32.15°N	70.0°W, 31.15°N	69.0°W, 30.15°N	68.0°W, 29.15°N
Interpreted stage	II-III-IV	II-III-IV	II-IV	II-IV	II-IV
Deepest shock (km)	245	283	234	238	261
Subhorizontal deep shocks	–	–	–	–	–

Listed for each cross section are the positions of the two end points of the profile, interpreted stage of slab subduction, depth of the deepest shock in km and observation of the subhorizontal distribution of deepest shocks (Yes if observed).

Li and van der Hilst [2010], and *Simmons et al.* [2012]). The slab is regarded as being at Stage I: slab stagnation in the transition zone (as summarized in Table 1). However, the stagnant slab configuration across northern Bonin is very different from that across Honshu, as the slab across northern Bonin dips more steeply and bends more sharply above the 660 horizon. This bend is associated with the corresponding bend of the hypocentral distribution, as observed in cross sections G–J in Figure 3 (see also Table 1).

[8] Figure 4 shows successive southward cross sections across the southern Bonin arc (A–E) and across the northern Mariana arc (F–J). Beneath the southern Bonin arc, the slab is stagnant above the 660. In cross sections A–D, the deepest hypocenters extend horizontally within the stagnant slab over a distance of 100–200 km from its trailing edge (see Table 1). Thus, the deepest seismicity bends in a way that is consistent with the tomographic images of the slab along the Bonin arc, all the way from its northern to its southern part. This implies that near the bending portion, the stagnant slab is brittle enough to cause earthquakes. This feature is consistent with recent finding: that near the bending portion, the stagnant

slab can be torn apart in a laterally extensional environment [*Obayashi et al.*, 2009].

[9] In Figure 4, the successive southward cross sections across the northern Mariana arc (F–J) show the images of a progressively deepening slab across the 660. We interpret this feature as indicating a process subsequent to the one occurring in southern Bonin (A–E). Although the resolution for the Mariana sections is more limited than for the Bonin sections, their progressive southward variation seems to suggest that the steeply down-dipping slab begins to penetrate the 660 near its deflection point, by leaving the horizontally deflected slab (stagnant slab) above the 660. This idea is consistent with the deepest seismicity in cross sections E–G, which extends vertically without bending (or with bending slightly backward as in cross section F). The cross section G depicts the deepest shock in the vicinity of the 660 km. As shown in this and other cases, the deepest shocks at depths 660 ± 40 km are diagnostic of slab penetration (Table 1). These earthquake mechanisms are of the downdip compression type [*Alpert et al.*, 2010] and, in general, are consistent with tomographic images of the slabs penetrating
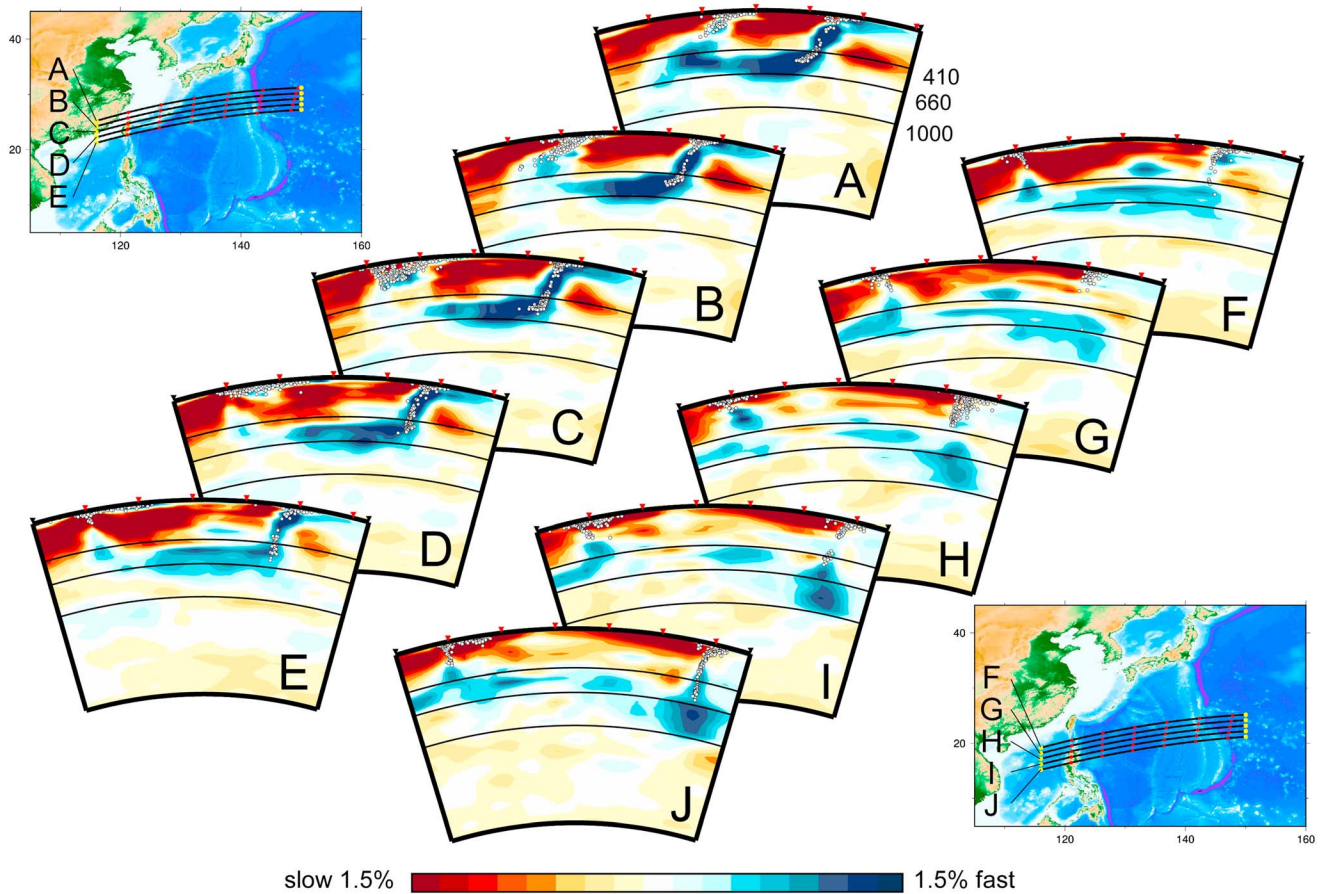
Figure 4. Successive slices of slab images. (top, left) Across the southern Bonin arc along profiles A–E shown in the top left map. (bottom, right) Across the northern Mariana arc along profiles F–J shown in the bottom right map. Other features are the same as those explained in Figure 3.

the 660, well into the uppermost lower mantle. Sections near the southern end of northern Mariana (I and J) indicate that the penetrated slab tends to be trapped in the uppermost lower mantle at depths above approximately 1000 km (see also *Kennett and Gorbatov* [2004]). Figure 5 shows a sketch illustrating the progressive change in slab configuration along the Japan arc to the northern Bonin, southern Bonin, and northern Mariana arcs.

3.2. Kurile

[10] Figure 6 shows successive northeastward cross sections across the southern Kurile arc (A–E) and across the northern Kurile arc (F–J). (Relevant references other than *Zhao et al.* [2010] are included within those cited in the previous section.) In the southern Kurile, cross section A shows a typical stagnant slab image. As we move further to the northeast, the bottom of the downgoing slab deepens progressively into the lower mantle across the 660. The horizontal part of the slab (stagnant slab) apparently remains above the 660 and is progressively thinned northeastward along the arc. Cross sections F–J appear to indicate the subsequent
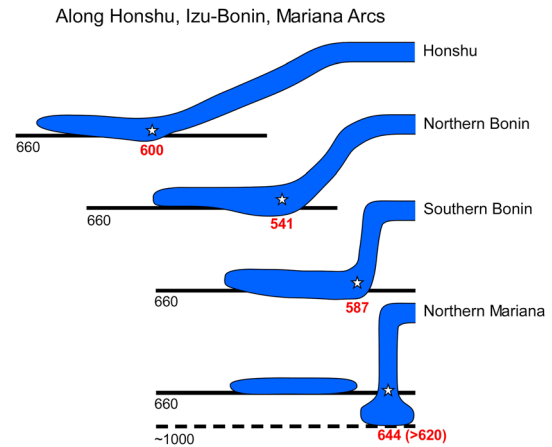
Figure 5. Sketch illustrating the progressive southward change in slab configuration, from the Honshu arc to the northern Bonin, southern Bonin, and northern Mariana, arcs. The numbers indicate the depth of the deepest shock beneath each arc (see Table 1 for more detail).
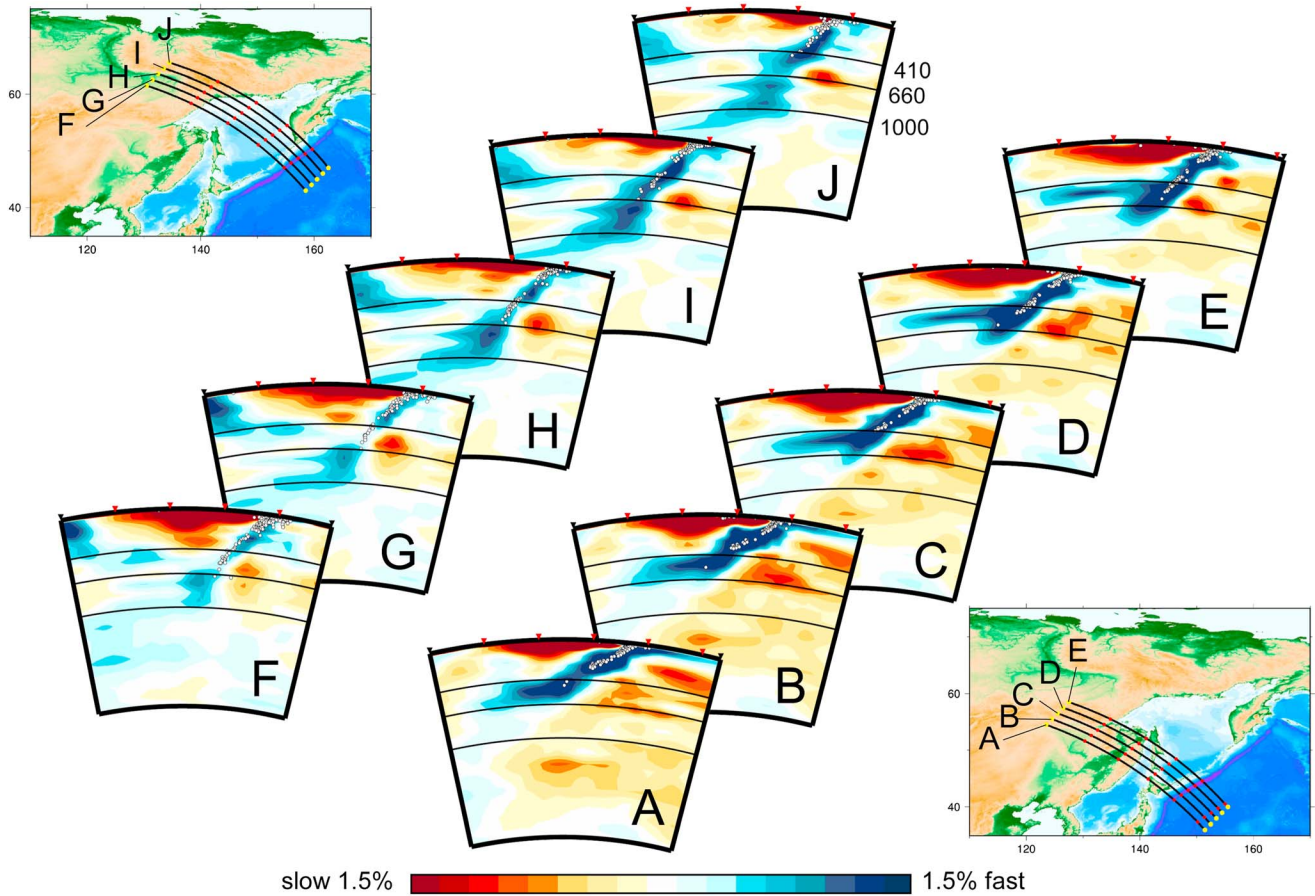
Figure 6. Successive slices of slab images. (bottom, right) Across the southern Kurile arc along profiles A–E shown in the bottom right map. (top, left) Across the northern Kurile arc along profiles F–J shown in the top left map. Other features are the same as those explained in Figure 3.

process occurring after the horizontal slab becomes too thin to be resolved. After penetration, the downgoing slab is progressively thickened in the uppermost lower mantle, with a tendency of being flattened near the bottom. Cross sections F–I show that the deepest shocks are located in the vicinity of the 660 km discontinuity (see Table 1). As pointed out in section 3.1, such deep shocks (660 ± 40 km) are diagnostic of slab penetration (Table 1). In each section, the deepest shocks are aligned very steeply. Their downdip compression mechanisms [*Alpert et al.*, 2010] indicate significant resistance against slab penetration across the 660. Figure 7 shows a sketch illustrating the progressive change in slab configuration along the Kurile arc, from its southern to northern part.

3.3. Java

[11] Figure 8 shows the successive westward cross sections across the Java arc, beneath which the Indo-Australian plate is subducted. (See *Fukao et al.* [2001] for earlier references to the Java slab images, including those of *Widiyantoro and van der Hilst* [1996]. See also *Replumaz et al.* [2004], *Li et al.* [2008], *van der Meer et al.* [2009], and *Widiyantoro*
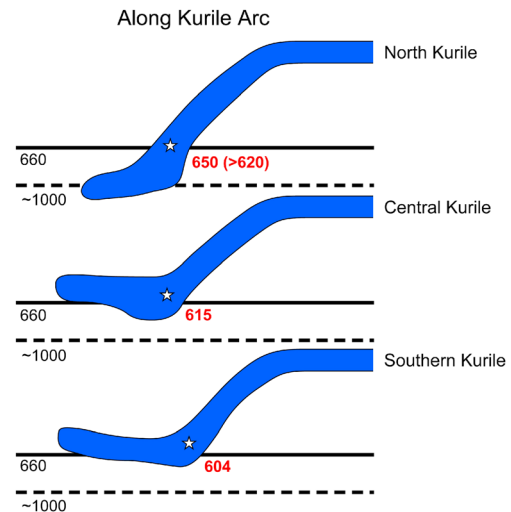

Figure 7. Sketch illustrating the progressive northward change in slab configuration from the southern to northern Kurile arc. The numbers indicate the depth of the deepest shock beneath each arc (see Table 1 for more detail).
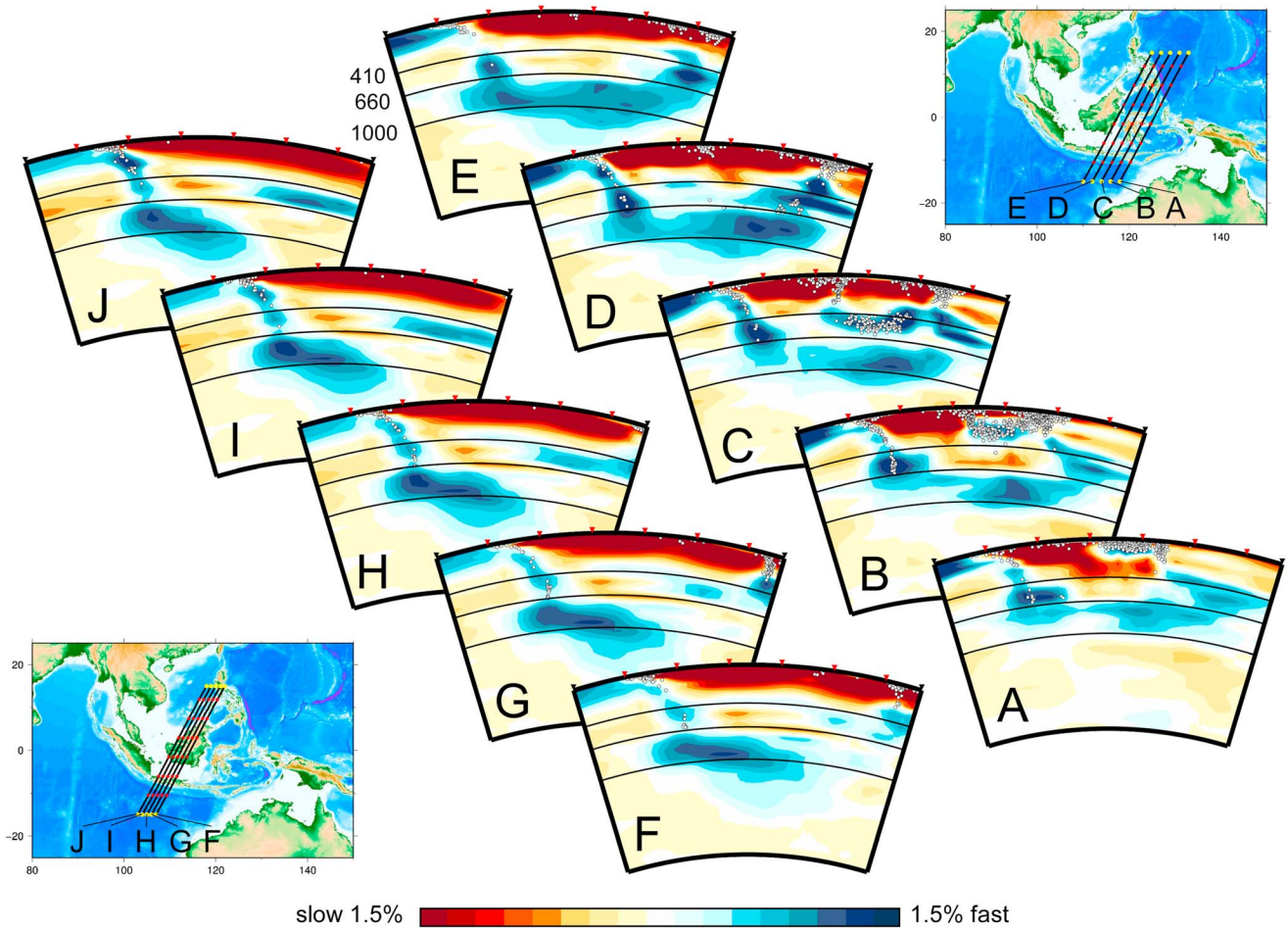
Figure 8. Successive slices of slab images. (top, right) Across the eastern Java arc along profiles A–E shown in the bottom right map. (bottom, left) Across the western Java arc along profiles F–J shown in the top left map. Other features are the same as those explained in Figure 3.

et al. [2011]). The slab feature differs between the eastern part (Flores and Sumbawa) and the western part (Java). In the eastern part, the slab: is stagnant above the 660 (section A, and sections further to the east (not shown)); begins to penetrate the 660 (section B); penetrates it well (sections C and D); and then starts to be trapped in the uppermost lower mantle (section E) (see Table 1). The stagnant slab feature in section A is consistent with that of the subhorizontal distribution of the deepest shocks. In the western part (sections F–J), the slab penetrates the 660 and is trapped typically in the uppermost lower mantle, where it spreads not only in a forward direction but also slightly in a backward direction [see *Hafkenscheid et al.* 2001, Figure 6]. It is intriguing that the deep hypocentral distribution (at depths greater than ~500 km) here dips steeply and slightly backward (southward), as clearly observed in sections F–H. This peculiar hypocentral distribution is consistent with the slightly backward alignment of the downdip compressional axes in the focal mechanisms of relevant deep shocks [*Schöffel and Das*, 1999; *Das et al.*, 2000]. The backward spread of the trapped slab, and the backward dipping of the downgoing slab, implies that these deeper and shallower parts of the slab are continuous across the 660. It is possible that the advance of the Java trench [*Funiciello et al.*, 2008] is responsible for
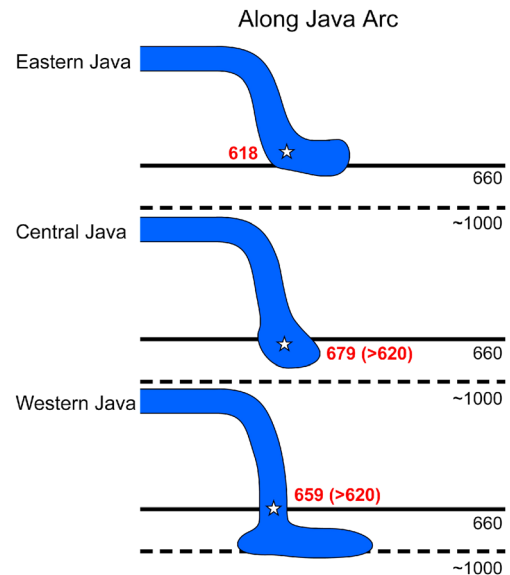

Figure 9. Sketch illustrating the progressive westward change in slab configuration from the eastern to western Java arc. The numbers indicate the depth of the deepest shock beneath each arc (see Table 1 for more detail).
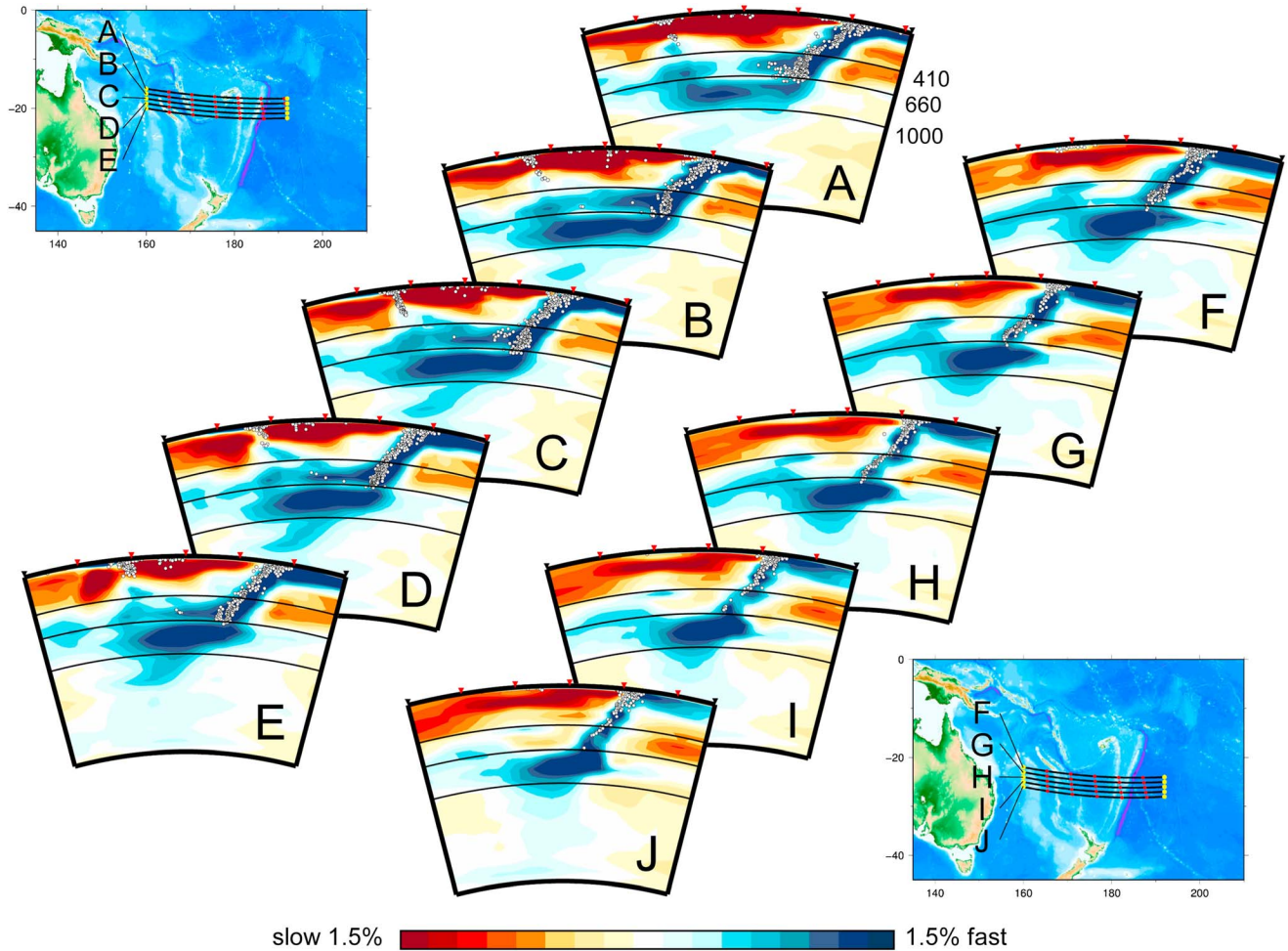
Figure 10. Successive slices of slab images. (top, left) Across the Tonga arc along profiles A–E shown in the top left map. (bottom, right) Across the Kermadec arc along profiles F–J shown in the bottom right map. Other features are the same as those explained in Figure 3.

the backward dipping of the downgoing slab with its bottom anchored in the uppermost lower mantle. Cross sections F–J appear to indicate that in western Java, the trapped slab in the uppermost lower mantle begins to extend its leading edge further deep into the lower mantle.

[12] In eastern Java, cross sections A–E show an additional complexity due to the penetration of the subducted slab of the Philippine Sea plate across the 660, and its trapping in the uppermost lower mantle, although the projections are not properly oriented for viewing this feature. The trapped slabs of the Indo-Australian plate and the Philippine Sea plate meet each other beneath the Celebes Sea (section E). Table 1 lists the depth of the deepest shock in each cross section across the Java arc. As pointed out in sections 3.1 and 3.2, the proximity of the hypocenters of these deepest shocks to the 660 (660 ± 40 km) is indicative of the slab penetration. Their downdip compression mechanisms [*Schöffel and Das*, 1999; *Alpert et al*., 2010] suggest some resistance against slab penetration across the 660. Figure 9 is a sketch illustrating the progressive change in slab configuration along the eastern to western Java arc. A three-dimensional view of

several slabs subducting complexly beneath the Sunda block was given by *Richards et al*. [2007], who configured the upper surface of the subducted slab by appropriately combining the hypocentral distribution of deep shocks and slab images in several *P* wave tomographic models.

3.4. Tonga-Kermadec

[13] Figure 10 shows successive southward cross sections across the Tonga-Kermadec arc. Here sections A–E are called the Tonga sections, and those from F–J are called the Kermadec sections. (See *Fukao et al*. [2001] for earlier references to Tonga slab images, including *van der Hilst* [1995]. See also *Hall and Spakman* [2002].) The Tonga sections (A–E) show the stagnant slab above the 660 and the penetrated slab below the 660 simultaneously. The deep seismicity also splits into two zones, in accord with the split images of the subducted slabs. Cross sections showing deep seismicity subparallel to the 660 horizon are marked in Table 1. More detailed studies of the deep seismicity and focal mechanisms [e.g., *Brudzinski and Chen*, 2005; *Bonnardot et al*., 2009] seem to suggest that the stagnant
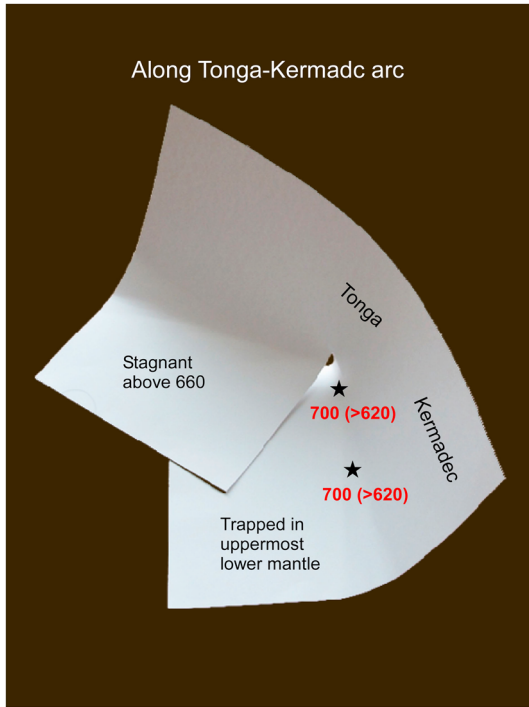
Figure 11. Origami illustration to explain tearing and consequent doubling of the slab in its deep part associated with the lateral bend of the Tonga slab. Doubling causes one slab to become stagnant above the 660 and the other to be trapped in the uppermost lower mantle. The latter-mentioned slab continues southward as the trapped slab beneath the Kermadec. The numbers indicate the depth of the deepest shock beneath each arc (see Table 1 for more detail).

slab above the 660 is the southwestward extension of the downgoing slab beneath the Lau basin and that the penetrated slab below the 660 is the westward extension of the downgoing slab from the southern Tonga trench. This situation is explained in Figure 11 using an origami illustration, which is not intended to imitate the real slab configuration but to illustrate the lateral bend of the stagnant slab and the consequent juxtaposition of the Tonga slab. Unlike in this origami illustration, the bent portion of the tomographic slab image lacks its shallower part at depths less than ~400 km. Noting this apparent lack, *Richards et al*. [2011] interpreted the stagnant slab above the 660 as a slab remnant detached from the Vanuatu trench, rather than from the northern Tonga trench. Deep shocks within the stagnant slab in the transition zone are characterized by slab-parallel compression mechanisms, such that the compressional axes are oriented on average at an azimuth of $262°$ and at an extremely shallow dip of $5°$ in the northern part, and at an azimuth of $309°$ and at a relatively shallow dip of $18°$ in the southern part [*Bonnardot et al*., 2009]. These mechanisms imply that the surrounding mantle is resisting the subhorizontal advance of the stagnant slab.

[14] The trapped slab in the uppermost lower mantle is persistently observed further to the south in the Kermadec sections (Figure 10, F–J). As in the case of western Java

(Figure 8), after penetration the Kermadec slab spreads laterally through the uppermost lower mantle, not only in a forward (westward) direction but also slightly in a backward (eastward) direction. Cross sections D–J appear to indicate that the trapped slab in the uppermost lower mantle begins to sink deeper, further along in the downdip direction of the upper mantle slab. Table 1 lists the depth of the deepest shock in each cross section along the Tonga-Kermadec arcs. The depth systematically exceeds 650 km, again demonstrating the close correlation between the deep shock activity at depths greater than ~620 km and slab penetration. The downdip compression mechanisms of these earthquakes [*Brudzinski and Chen*, 2005; *Bonnardot et al*., 2009; *Alpert et al*., 2010] suggest that the surrounding mantle is resisting the slab penetrating the 660.

3.5. South America

[15] In this study we call the slabs of the Nazca plate to the north and south of the Peru-Chile border, the Peruvian slab and the Chilean slab, respectively. Figure 12 shows successive southward cross sections along the EW profiles of the Chilean slab, where we continually observe images of the stagnant slab above the 660. Earlier *P* velocity models that are consistent with these images include those of *Bijwaard et al*. [1998] and *Fukao et al*. [2001], as well as the most recent model of *Simmons et al*. [2012]. A recent model of *Li et al*. [2008] does not show an obvious stagnant slab feature, however. In the present study, the Chilean slab is imaged to be stagnant above the 660 all the way along the arc, yet its configuration differs significantly between the northern part (A–E) and the southern part (F–J) across ~25°S. This difference in configuration includes a difference in the dip of the slab image at shallow depths, which corresponds well to the dip difference of the intermediate-depth seismic zone. The seismic zone dips relatively steeply in the northern part ($25 \pm 5°$ according to *Brudzinski and Chen* [2005], see also *Martinod et al*. [2010]) but very shallowly in the southern part ($7 \pm 4°$ according to *Brudzinski and Chen* [2005], see also *Martinod et al*. [2010]). In the northern part, both the tomographic image and intermediate-depth earthquake distribution show an abrupt kink around a depth of ~250 km, below which the slab dips steeply, although the upper and lower portions of the slab appear to be continuous across this kink. In the southern part, however, the tomographic image and the seismicity seem to suggest that the upper portion is detached from the lower portion so that relative to the lower portion it independently advances further landward. The slab entering the transition zone spreads horizontally as a stagnant slab. Cross sections D and E indicate that the deepest hypocenters extend subhorizontally within the stagnant slab from its trailing edge, over a distance range of ~200 km, as noted in Table 1. This is a situation similar to that of the stagnant slabs in northern Bonin (Figure 3), southern Bonin (Figure 4), easternmost Java (Figure 8), and Tonga (Figure 10). This situation again implies that the stagnant slab remains seismically brittle, at least within some distance range from its trailing edge.

[16] The stagnant slab feature (as observed in the Chilean slab) does not extend northward into the Peruvian slab across the slab-slab junction. Figure 13 shows successive northward cross sections A–E and F–J of the Peruvian slab images. See
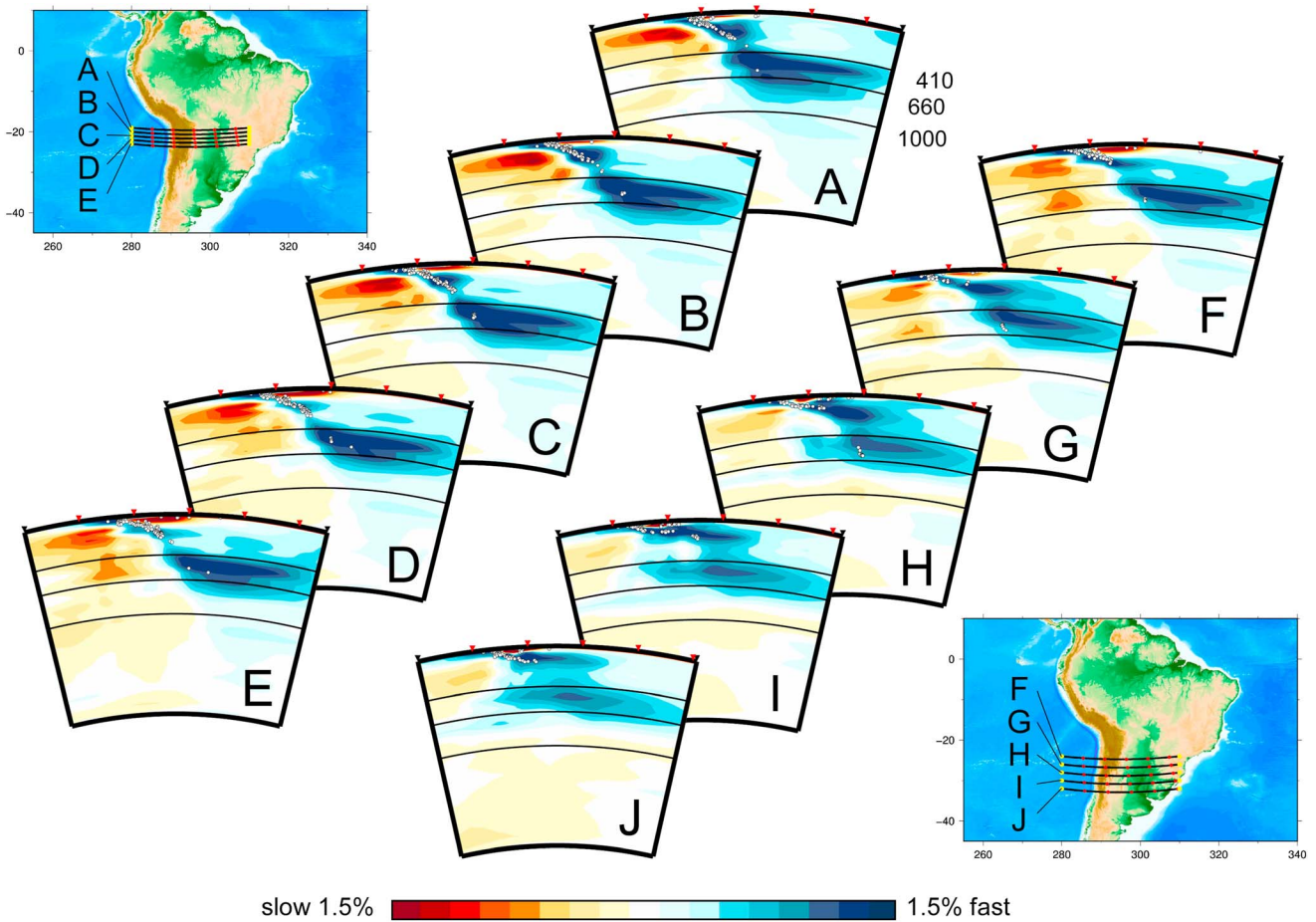
Figure 12. Successive slices of slab images. (top, left) Across the northern part of the Chilean continental arc along profiles A–E shown in the top left map. (bottom, right) Across the central part of the Chilean continental arc along profiles F–J shown in the bottom right map. Other features are the same as those explained in Figure 3.

Fukao et al. [2001] for earlier references to the Peruvian slab images, including *Engdahl et al.* [1995]. (See also *Ren et al.* [2007], *Li et al.* [2008], and *Simmons et al.* [2012]). Cross sections from A to E show slab images in the transitional stages, from the subhorizontal slab above the 660 to that below it. The deepest shocks in sections D and E are both at depths of 640 km, thoroughly exceeding 620 km, and are diagnostic of slab penetration. Note that the vertical spread of the slab image in these cross sections is largely an artifact due to the slab contortion across the Peru-Chile border, where the slab is dipping to the north rather than to the east (see Figure 14). The EW alignment of the deepest shocks, as observed in cross sections D and E, is also an artifact, due to the locally northward dipping nature of the slab (not remarked on in Table 1 accordingly). Cross sections F–J clearly show the images of the slab as it penetrates the 660 and then deflects to be trapped in the uppermost lower mantle. The leading edge of the trapped slab seems to begin to submerge further down. Seismic activity is very high within the penetrating slab in the proximity of the 660 (cross sections G–J; see also Table 1). Although this deepest seismicity is well isolated from the shallower seismicity [see

Brudzinski and Chen, 2005; *Martinod et al.*, 2010], the tomographic cross sections seem to suggest that the slab involving this seismicity is not detached but continues from the presently subducting shallow slab of the Nazca plate (at least to the south of 10°N). Earthquakes occurring at the greatest depths are of the downdip compression type, with steep compressional axes (average plunge = 79°) [*Brudzinski and Chen* 2005]. This again suggests that the surrounding mantle is resisting the penetration of the slab across the 660.

[17] We have observed a significant contrast in the slab configuration between southern South America (Chilean slab: Figure 12) and northern South America (Peruvian slab: Figure 13). Figure 14 shows this contrast in a cross-sectional view along the north-south profiles. In southern South America, the slab is persistently stagnant above the 660, while in northern South America, the slab is persistently trapped in the uppermost lower mantle. This change of slab configuration, from the Chilean to Peruvian type, occurs across the arc-arc junction where the slab forms a plateau. The northern flank of this E-to-NE-oriented plateau of the slab has the following features: It is steeply sloping to the north, then encounters the 660, generates the deepest
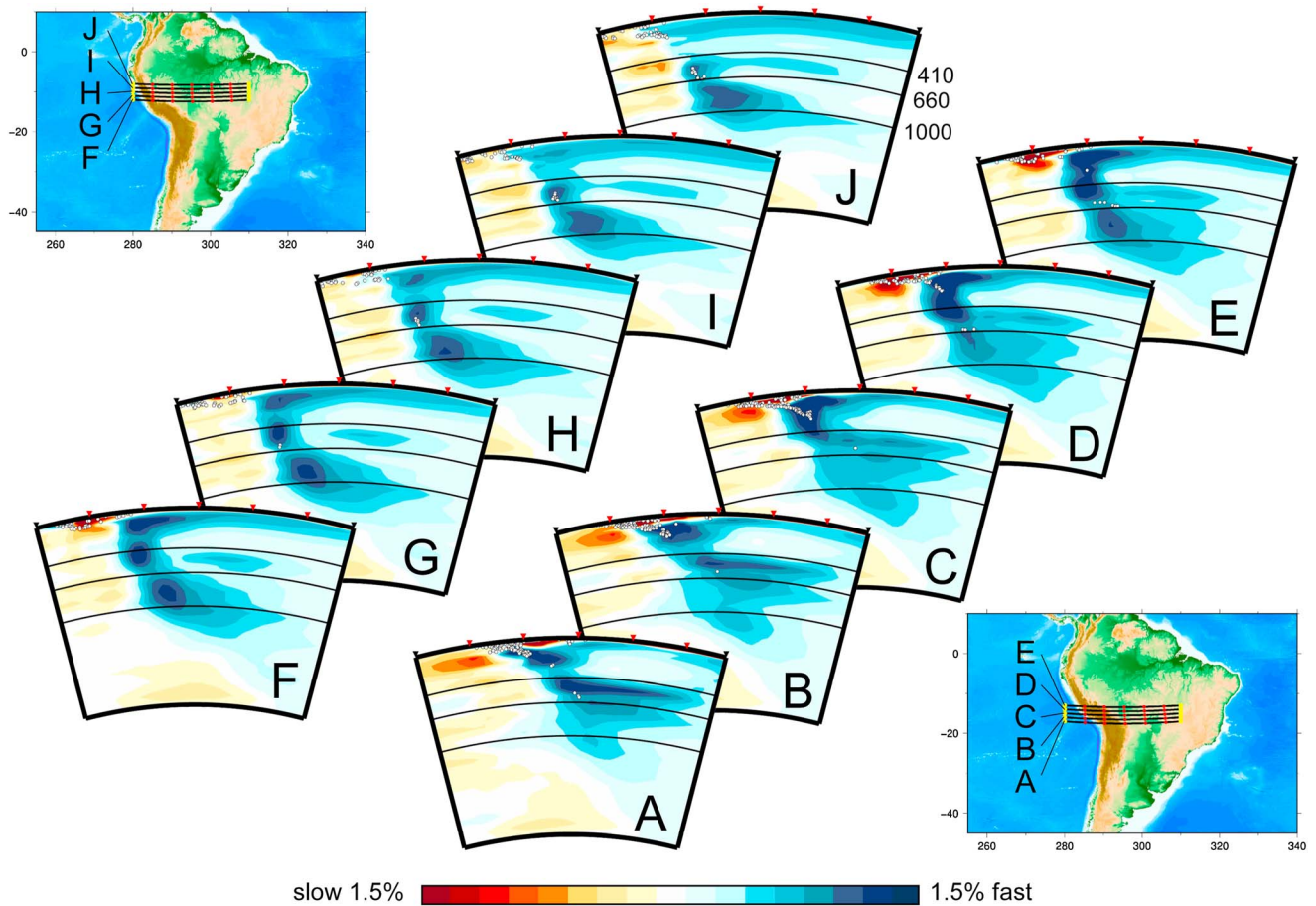
Figure 13. Successive slices of slab images. (bottom, right) Across the southern part of the Peruvian continental arc along profiles A–E shown in the bottom right map. (top, left) Across the northern part of the Peruvian continental arc along profiles F–J shown in the top left map. Other features are the same as those explained in Figure 3.

earthquakes at depths of around 660 km, penetrates the 660 km discontinuity, and thereby connects to the Peruvian trapped slab in the uppermost lower mantle. This unique local slab configuration appears to be consistent with the focal mechanisms of the deepest shocks in this region (a typical example of which is taken from the Global Centroid-Moment-Tensor (gCMT) catalog (Global CMT Project, 2006) (formerly Harvard CMT), available at http://www.globalcmt.org/, accessed May 2008) and is shown in Figure 14. The *P* axis of this event is consistent with its interpretation as being a downdip compression within the locally northward dipping slab. The slab configuration in this region is explained in Figure 15 using an origami illustration, which is not intended to imitate the real slab configuration but to suggest a possible slab continuation across the junction from the Chile to Peruvian slab, where the slab to the south is stagnant in the transition zone and the slab to the north is trapped in the uppermost lower mantle.

3.6. Central America

[18] Tomographic images of the slab deeply subducted in the lower mantle in this region have been repeatedly reported [*Grand*, 2002; *Ren et al.*, 2007; *Li et al.*, 2008; see *Fukao et al.*, 2001 for the earlier references including *van der Hilst et al.* [1997] and *Grand et al.* [1997]]. Figure 16 shows the successive southward cross section across Central America. The northernmost cross sections show the slab penetrating the 660 and trapped in the uppermost lower mantle. As we move southward, the trapped slab progressively changes its configuration and increases its average dip, becoming a slab deeply penetrating through the lower mantle. In cross sections F–J, the slab at intermediate depths is imaged as being one with higher-than-surrounding velocities associated with intermediate-depth seismic activity; suggesting a continuation of the slab all the way from the shallow to lower mantle. Although the shallow subduction is not clearly imaged in cross sections A and B, and is not even represented by higher-than-surrounding velocities, the connection between the shallow and deep subduction can be observed in the tomographic work by *Gorbatov and Fukao* [2005], who used an extensive regional data set in addition to the global data set. According to *Gorbatov and Fukao* [2005], the slab image further to the north of the northernmost cross section A is split into the shallow and deep
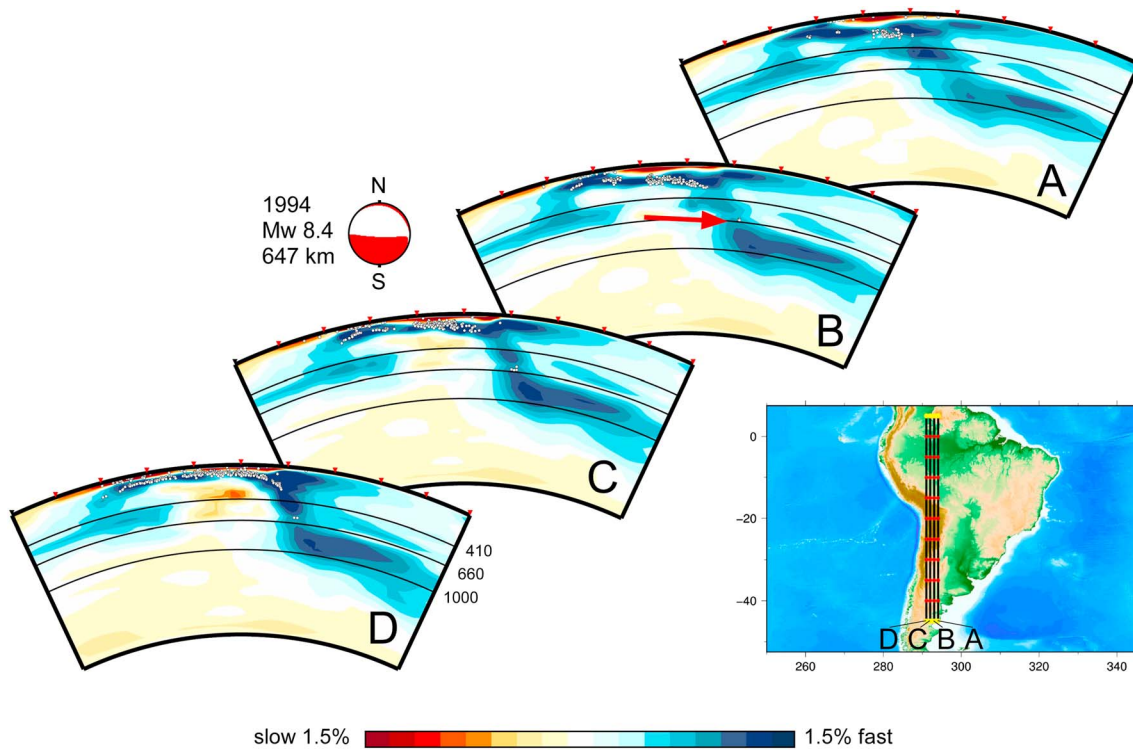
Figure 14. Successive slices of slab images along north-south profiles A–D shown in the map at the bottom right. Here a significant contrast is observed in the slab configuration between the Peruvian and Chilean segments. Also shown is the focal mechanism of a deepest shock occurring in the Peru-Chile junction region in an equal-area projection of the lower half of the focal sphere, where the shaded quadrants represent the compressional first motions. Other features are the same as those explained in Figure 3.

parts, with a significant gap between the two. The shallower part is the subducting slab of the Cocos plate, now stagnant above the 660, and the deeper part is interpreted as being the remnant slab of the Farallon plate still trapped in the uppermost lower mantle, which appears to continue further to the north up to 35°N where it is then truncated by the eastward continuation of the Mendocino fracture zone [*Sigloch et al.*, 2008; *Sigloch*, 2011]. Figure 17 shows a sketch of the slab configuration change along Central America, from its northern to middle part. In the sketch, cross sections A–J are interpreted as being successive snapshots of the clockwise rotation of the slab.

4. Discussion

[19] We have observed systematic along-arc lateral variations in slab configuration for each of the major subduction zones around the circum-Pacific. We interpret this lateral variation as indicating the progressive descent of the slab through the mantle transition region at a depth range of 400–1000 km. The stages of slab decent are as follows: the subducted slab is stagnant above the 660 (Stage I); the stagnant slab then penetrates the 660 (Stage II); the penetrated slab is subsequently trapped in the uppermost lower mantle, although its bottom is only vaguely defined at around ~1000 km (Stage III); the trapped slab eventually descends into the deep lower mantle (Stage IV). There may be a case,

however, where a downgoing slab bypasses stage I and enters directly into stage II or where a penetrated slab bypasses stage III and enters directly into stage IV.

[20] Figure 18 is a collection of typical pairs of tomographic images of a stagnant slab (left) and a trapped slab (right) in the same subduction zone. We interpret each pair as being at Stage I and III, respectively. This figure exhibits the remarkable correlation of deep slab configuration with the distribution of deepest earthquakes. The subhorizontal distribution of deepest shocks is associated with a stagnant slab in the transition zone (slab at Stage I). The steeply dipping distribution is associated with a penetrating slab across the 660 or a trapped slab below it (slab at Stage II or III). There are no cases of association of either a stagnant slab (at Stage I) with the subvertical distribution of deepest shocks, or a trapped slab (at Stage II or III) with the subhorizontal distribution. Only steeply dipping slabs appear to penetrate the 660 to be trapped in the uppermost lower mantle. As in the cases of Mariana (Figure 4) and Kurile (Figure 6), the stagnant part of the slab seems often to be left on the 660 when the downgoing part penetrates it.

[21] Table 1 summarizes the characteristics of slab images for all the cross sections, including our interpretations. Figure 19 is the outline of this table. Most of the slabs are either at Stage I or III. The Central America slab is the only slab definitely identified as being at Stage IV, at least among the slabs we surveyed. In view of the observed frequency of
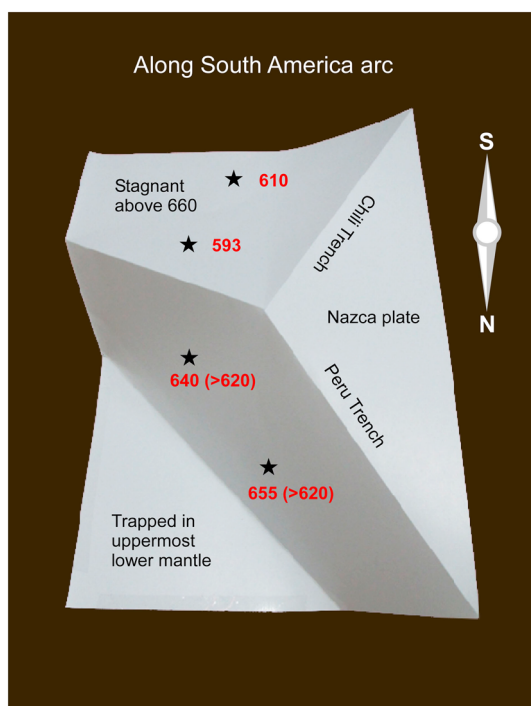
Figure 15. Origami illustration for the slab configuration change across the arc-arc junction of South America, viewed from north. The Chilean slab to the south of the junction is stagnant above the 660, and the Peruvian slab to the north is trapped in the uppermost lower mantle. The two slabs are continuous across their junction at least at depths above the 660 km discontinuity. The numbers indicate the depth of the deepest shock beneath each arc (see Table 1 for more detail).

cases, we regard Stages I and III as being relatively stable or neutral stages and II and IV as being relatively unstable, transient stages. Stages I and III suggest that there are two slab reservoirs in the mantle transition region, one above the 660 and the other just below it, although neither is a perfect barrier to further slab decent. This dual nature of the slab reservoirs in the mantle across the 660 has also been demonstrated in the global map view in Figures 1b, 1c, and 1d.

[22] In Figure 19, a cross section showing the subhorizontal distribution of deepest shocks within the slab is marked by the corresponding cross-section letter. The subhorizontal hypocentral distribution is, in general, associated with a stagnant slab in the transition zone, not with a trapped slab in the uppermost lower mantle, as we have already observed in Figure 18. Figure 19 also shows the depth of the deepest shock in each cross section. The depth is given in black if it is shallower than 620 km and in red if deeper than 620 km. This depth classification clearly distinguishes penetrated slabs from stagnant slabs. The deepest seismic activity at depths greater than ~620 km is a good measure of the presence of a slab penetrating the 660. The downdip compression nature of deepest earthquakes [*Brudzinski and Chen*, 2005; *Bonnardot et al.*, 2009; *Alpert et al.*, 2010], and the

steeply dipping nature of the slab at Stage II or III near the bottom of the transition zone (Figure 18), implies that the surrounding mantle is resisting the slab penetration.

[23] Figure 20 delivers an explanation of this situation with reference to the Tonga-Kermadec arc, where deepest earthquakes occur at depths ~700 km well below the nominal depth of the 660 km discontinuity. The location of the 660 km discontinuity in the Tonga-Kermadec region, estimated by the S-to-P converted waves, lies at depths as deep as 730 km in the central part of the slab, then shallows progressively outward and returns to the normal depth of 660 km well outside of the slab [*Niu and Kawakatsu*, 1995]. The boundary depth of 730 km implies the boundary depression of 70 km from the 660, which is much deeper than the experimentally expected phase boundary depth of postspinel transition at equilibrium. The experimental Clapeyron slope is reported to be $dP/dT = -1.3$ MPa/K for Mg_2SiO [*Fei et al.*, 2004], with which the 660 km depression is predicted to be only 16 km for a cold temperature anomaly of 500 K. The seismologically observed excess depression may be explained by a kinetically retarded postspinel transition [*Kubo et al.*, 2002a, 2002b]. The retarded phase transition would widen the buoyant part of the slab downward and hence the downdip-compression domain of the slab [*Bina*, 1996], which would generate deep shocks at depths greater than expected from the equilibrium phase transition.

[24] Many numerical modeling studies have focused on the processes occurring at Stages I and II across the 660, where the postspinel phase transition takes place and a viscosity jump may occur as well [*Billen*, 2008; *Fukao et al.*, 2009; *Yanagisawa et al.*, 2010]. None of these studies, however, have directly addressed the processes occurring at Stage III, although some have shown a case of the slab undergoing subhorizontal bent below the 660 [*Christensen*, 1996; *Torii and Yoshioka*, 2007] (see *Fukao et al.* [2009] for other references), including a case of the slab buckling directly below its penetration point [*Christensen*, 1996; *Ribe et al.*, 2007; *Stegman et al.*, 2010]. These numerical experiments suggest that the postspinel phase transition and the viscosity jump across the 660 alone are unable to explain stage III as a generally occurring process of slab descent. In addition, although trench retreat is one of important factors controlling deep slab configuration [*van der Hilst and Seno*, 1993], there seems to be no systematic correlation between deep slab configuration and ongoing trench migration in any global reference model [*Funiciello et al.*, 2008; *Schellart et al.*, 2008].

[25] Reflection analyses of seismic waves from deep shocks have detected seismic reflectors associated with penetrated slabs. These reflectors have been attributed to fragments of the subducted oceanic crust (see *Fukao et al.* [2009] for discussion and references). Because these fragments are mostly located well inside the penetrated slab [e.g. *Kaneshima*, 2003, 2009] or even at the bottom [*Niu et al.*, 2003], they seem to have been displaced from their original positions at the top of the slab through severe internal deformation. The internal deformation is likely to be due to slab softening associated with the postspinel transition, which would also explain the abrupt cessation of deepest seismicity at a depth of 700 km, rather than at 660 km (Figure 20, Table 1). The possible softening mechanism includes superplasticity due to a grain size
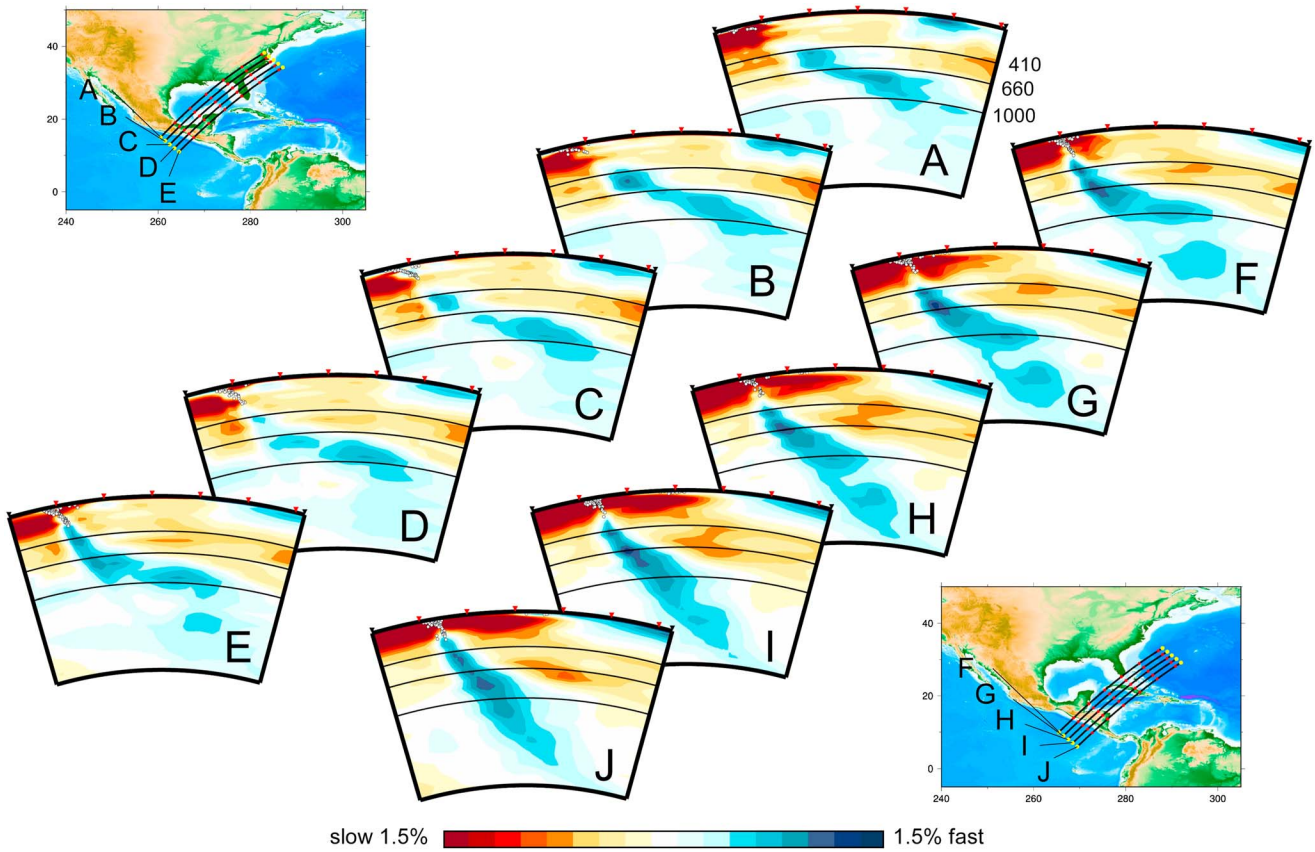
Figure 16. Successive slices of slab images. (top, left) Across the northern part of the Central America arc along profiles A–E shown in the left top map. (bottom, right) Across the middle part of the Central America arc along profiles F–J shown in the right bottom map. Other features are the same as those described in Figure 3.

reduction associated with the phase transition [*Ito and Sato*, 1991] and/or softening due to networking of a very soft ferropericlase phase through the matrix of a perovskite phase [*Yamazaki et al.*, 2009]. The softened slab might easily be deflected to a shallower dip upon its descent through the more viscous surrounding mantle, to become trapped in the uppermost lower mantle, although the detailed process is poorly understood. This is a possible mechanism attributing the subhorizontal deflection of the slab below the 660 to the internal process occurring within the slab. Alternatively, one might consider a mechanism that is associated with a structural barrier outside the slab. Joint inversion of convection-related data and glacial isostatic adjustment data shows several viscosity profiles consistent with geophysical observations that have a relative maximum at depths around 1000 km [*Mitrovica and Forte*, 2004]. Such a viscosity maximum would allow the slab to deflect horizontally in the uppermost lower mantle and then to sink further deep [*Morra et al.*, 2010]. Although the mechanisms are poorly understood, it is almost certain that the uppermost lower mantle acts as a slab reservoir. Slabs may remain trapped in the uppermost lower mantle even
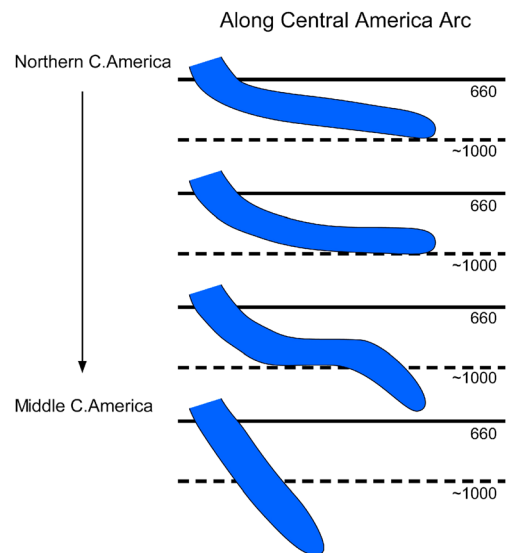

Figure 17. Sketch illustrating the progressive southward change in slab configuration from the northern to middle Central America arc.
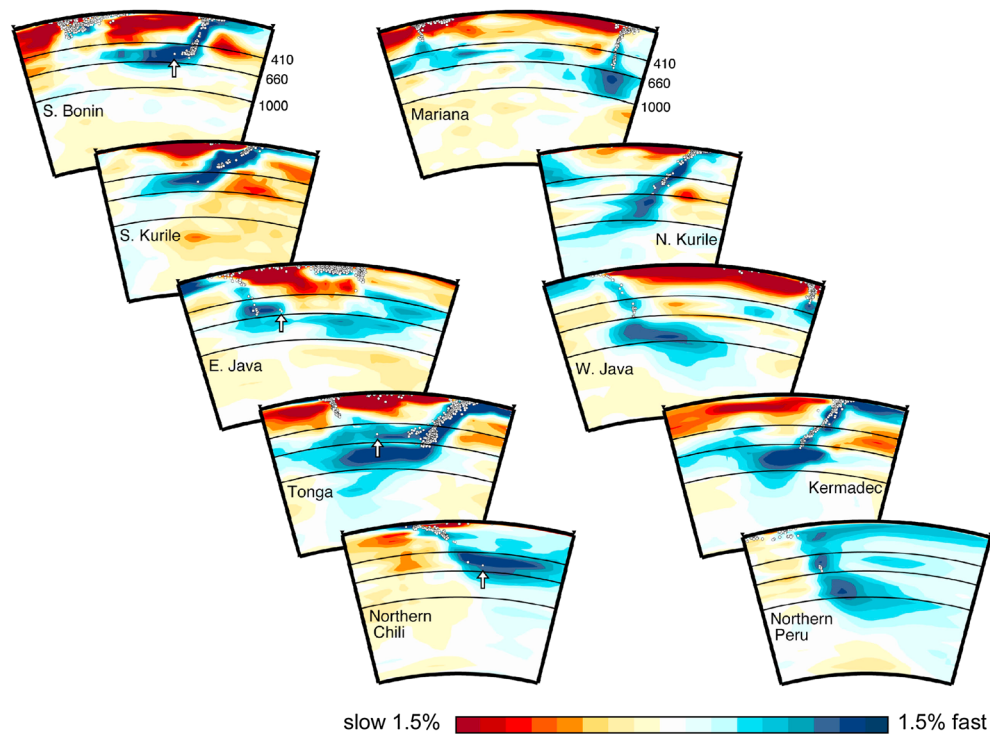
Figure 18. Images of a stagnant slab in the transition zone (left) and of a trapped slab in the uppermost lower mantle (right) in the same subduction zone. Five subduction zones are selected in this illustration. Subhorizontal distributions of deepest shocks as marked by arrows are associated with stagnant slabs in the transition zone. Steeply dipping distributions are associated with penetrating slabs across the 660 or with trapped slabs below it.

after cessation of slab subduction in the upper mantle. Indeed, the slab remnants of the Farallon plate are still widely observed in the uppermost lower mantle under North America [*Sigloch and Mihalynuk*, 2013].

5. Conclusions

[26] Our systematic survey of slab images around the circum-Pacific shows the systematic variations of slab configurations implying that subducting slabs are in one or two of the following four stages:

[27] 1. I. Slab is stagnant above the 660.

[28] 2. II. Stagnant slab penetrates the 660.

[29] 3. III. Penetrated slab is trapped in the uppermost lower mantle.

[30] 4. IV. Trapped slab descends well into the deep lower mantle.

[31] We interpret Stages I to IV as being the successive stages of slab subduction through the transition region (with the 660 at the middle), although there may be cases where a downgoing slab enters directly into Stage II by bypassing Stage I, or where a penetrated slab enters directly into Stage IV, thereby bypassing Stage III. These four stages indicate that not only the transition zone above the 660 but also the uppermost lower mantle below it acts separately as a reservoir of subducting slabs. There is a remarkable

Figure 19. Summary illustration showing the current stage (s) of a subducting slab. In the case of northern Mariana, the slab penetrates the 660 (bold bar), leaving the horizontal slab above the 660 (dotted bar). The numbers indicate the depth of the deepest shock within each slab. Red numbers indicate that the depth is greater than 620 km, which is always associated with penetrated slabs at Stages II or III. The cross section showing the subhorizontal bend of the deepest hypocentral distribution is marked by the corresponding cross-section letter, which is always associated with stagnant slabs at Stage I.
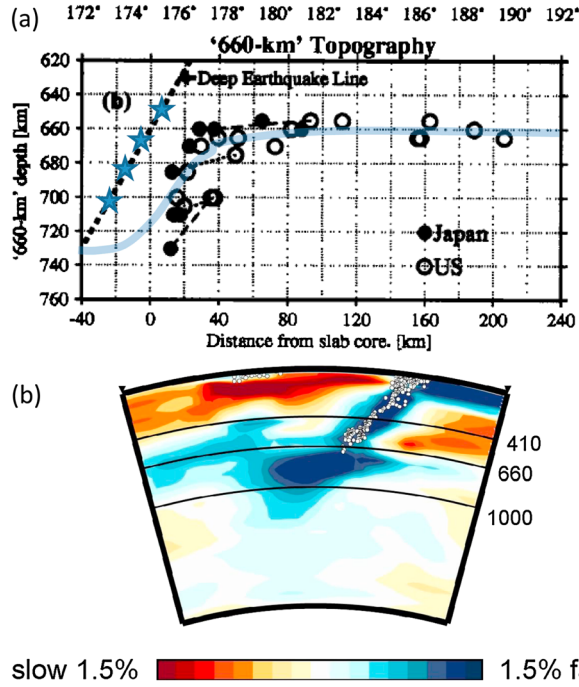
Figure 20. (a) Seismologically-determined phase boundary depths (closed and open circles) of the postspinel transition across the Tonga-Kerrmadec arc [*Niu and Kawakatsu*, 1995]. Dotted line represents the deep seismic zone, which is assumed to be the slab core. The pointwise estimated phase boundary depths are smoothly connected by the present authors. Deepest shocks (marked by stars) are schematically added by the present authors, and extend to depths of 700 km. (b) Tomographic cross section across the Kermadec arc (the same as cross section F in Figure 10).

correspondence between the images of deep slabs and the deepest hypocentral distributions. Stagnant slabs above the 660 (slabs at Stage I) are associated with the subhorizontal distribution of deepest shocks shallower than ∼ 620 km, and penetrated slabs at Stages II or III are accompanied by the very steeply dipping distribution of deepest shocks deeper than ∼ 620 km.

Appendix A: Resolution Test

[32] We computed the so-called point-spreading kernels for selected blocks that correspond to the column vectors of the resolution matrix [*Humphreys and Clayton*, 1988], in order to assess how well the slab images have been obtained. A point-spreading kernel shows to what extent a unit (1%) anomaly given to a selected block is recovered by the data. Because the mantle is not parameterized by uniform blocks but by the blocks of which size varies with the resolution expected by the data (a smaller block in the region where good resolution is expected), it is difficult to interpret the individual values of a point-spreading kernel. We thus consider the resolution on a $2.5° \times 2.5°$ lateral scale, which is 4 times as large as the smallest block and retain the layer thickness within the real tomography. Although the resolution on a smaller scale would be lower
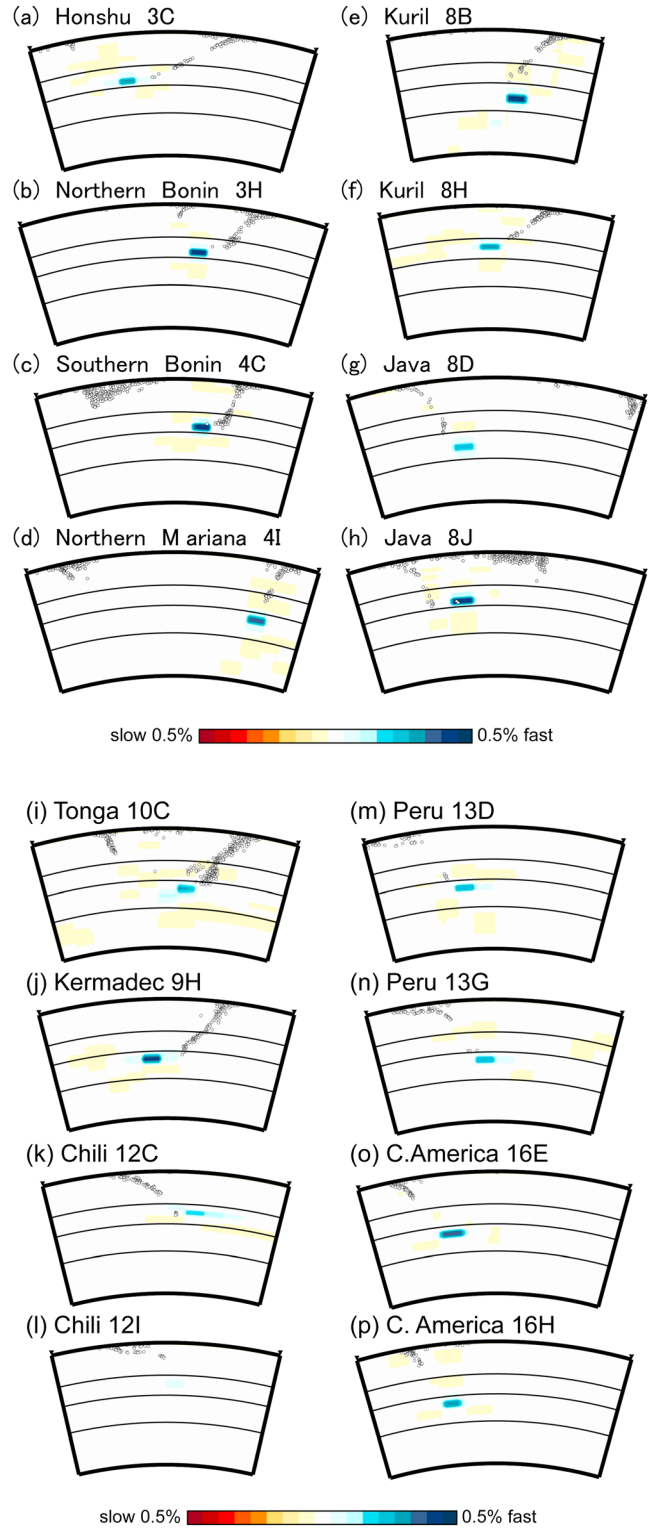

Figure A1. Point spreading kernels for selected target blocks. The letters indicate the cross section containing the target block and the numbers indicate the relevant figure number. The anomaly given to a target block is 1.0%.
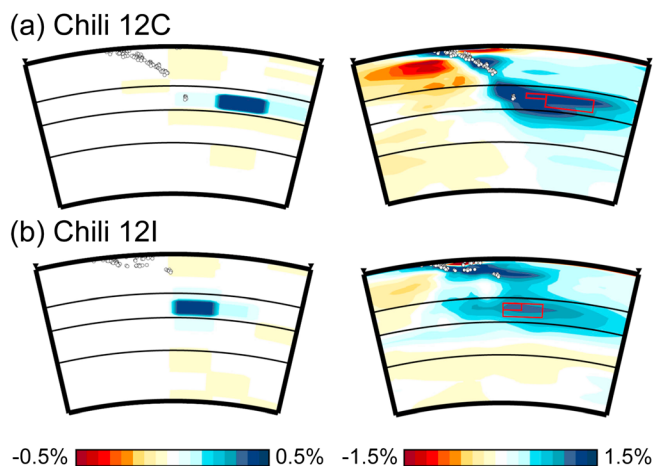
(a) Chili 12C

(b) Chili 12I

-0.5% ■■■■■ 0.5%   -1.5% ■■■■■ 1.5%

Figure A2. (left) Point spreading kernels for selected target blocks. The block size is twice the length and 8 times the volume of the one given in Figure A1. Only the Chile sections are shown. See Figure A1 for other explanations. (right) Locations and sizes of target blocks used for A1 and A2. The tomographic slab images are superposed.

than the one obtained in this test, the slab structure (which is our interest) is much larger than the test block size. Figure A1 shows several examples of the test results. In this figure, we select one from five of the across-arc cross sections in each of 16 regions along the circum-Pacific. The target block is chosen in the flattened part of the slab image in the case of a flattened slab and in the penetrated portion of the slab image in the case of a penetrated slab. In Figure A1, only the target block is of a relatively large positive value; therefore, we can easily recognize it from other blocks. This indicates that most target blocks are resolved on the relevant scale, even though the anomaly value of 1.0 given to the target block spreads considerably to the surrounding blocks. Exceptions are found in the Chile sections (k) and (l). In both these sections, the value recovered for the target block is much smaller than those in other cross sections. In section (k), in particular, the target anomaly spreads horizontally landward. Since our interest is the slab signature on a much larger scale, we tested the resolution for larger target blocks with a linear dimension twice as large as that in Figure A1. Figure A2 shows the results for the Chile sections (k) and (l), where the target block is now well resolved. We conclude that the resolution of our tomography is adequate for discussing slab morphology on a scale presented in either Figure A1 or A2.

References

Alpert, L. A., T. W. Becker, and I. W. Bailey (2010), Global slab deformation and centroid moment tensor constraints on viscosity, *Geochem. Geophys. Geosyst.*, *11*, Q12006, doi:10.1029/2010GC003301.
Andrews, J., and A. Deuss (2008), Detailed nature of the 660 km region of the mantle from global receiver function data, *J. Geophys. Res.*, *113*, B06304, doi:10.1029/2007JB005111.

Bijwaard, H., W. Spakman, and E. R. Engdahl (1998), Closing the gap between regional and global tomography, *J. Geophys. Res.*, *103*, 30,005–30,078.
Billen, M. I. (2008), Modeling the dynamics of subducting slabs, *Annu. Rev. Earth Planet. Sci.*, *36*, 325–356.
Bina, C. R. (1996), Phase transition buoyancy contributions to stresses in subducting lithosphere, *Geophys. Res. Lett.*, *23*, 3563–3566.
Bonnardot, M. A., M. Régnier, C. Christova, E. Ruellan, and E. Tric (2009), Seismological evidence for a slab detachment in the Tonga subduction zone, *Tectonophysics*, *464*, 84–99.
Brudzinski, M. R., and W.-P. Chen (2005), Earthquakes and strain in subhorizontal slabs, *J. Geophys. Res.*, *110*, B08303, doi:10.1029/2004JB003470.
Bullen, B. (1963), *Introduction to the Theory of Seismology*, 381 pp., Cambridge Univ. Press, New York.
Cao, Q., P. Wanga, R. D. van der Hilst, M. V. de Hoop, and S.-H. Shim (2010), Imaging the upper mantle transition zone with a generalized Radon transform of SS precursors, *Phys. Earth Planet. Inter.*, *180*, 80–91.
Christensen, U. R. (1996), The influence of trench migration on slab penetration into the lower mantle, *Earth Planet. Sci. Lett.*, *140*, 27–39.
Courtier, A. M., and J. Revenaugh (2008), Slabs and shear wave reflectors in the midmantle, *J. Geophys. Res.*, *113*, B08312, doi:10.1029/2007JB005261.
Courtier, A. M., B. Bagley, and J. Revenaugh (2007), Whole mantle discontinuity structure beneath Hawaii, *Geophys. Res. Lett.*, *34*, L17304, doi:10.1029/2007GL031006.
Dahlen, F., S.-H. Hung, and G. Nolet (2000), Fréchet kernels for finite frequency traveltimes–I. Theory, *Geophys. J. Int.*, *141*, 157–174.
Das, S., H.-J. Sch ffel, and F. Gilbert (2000), Mechanism of slab thickening near 670 km under Indonesia, *J. Geophys. Res.*, *27*, 831–834.
Engdahl, E. R., R. van der Hilst, and J. Berrocal (1995), Imaging of subducted lithosphere beneath South America, *Geophys. Res. Lett.*, *22*, 2317–2320.
Engdahl, E. R., R. van der Hilst, and R. Buland (1998), Global teleseismic earthquake relocation with improved travel times and procedures for depth determination, *Bull. Seismol. Soc. Am.*, *88*, 722–743.
Fei, Y., J. Van Orman, J. Li, W. van Westrenen, C. Sanloup, W. Minarik, K. Hirose, T. Komabayashi, M. Walter, and K. Funakoshi (2004), Experimentally determined postspinel transformation boundary in Mg2SiO4 using MgO as an internal pressure standard and its geophysical implications, *J. Geophys. Res.*, *109*, B02305, doi:10.1029/2003JB002562.
Forte, A. M., and J. X. Mitrovica (2001), Deep-mantle high-viscosity flow and thermochemical structure inferred from seismic and geodynamic data, *Nature*, *410*, 1049–1056.
Fukao, Y., M. Obayashi, H. Inoue, and M. Nenbai (1992), Subducting slabs stagnant in the mantle transition zone, *J. Geophys. Res.*, *97*, 4809–4822.
Fukao, Y., S. Widiyantoro, and M. Obayashi (2001), Stagnant slabs in the upper and lower mantle transition region, *Rev. Geophys.*, *39*, 291–323.
Fukao, Y., M. Obayashi, T. Nakakuki, and the Deep Slab Project Group (2009), Stagnant slab: A review, *Annu. Rev. Earth Planet. Sci.*, *37*, 19–46, doi:10.1146/annurev.earth.36.031207.124224.
Funiciello, F., C. Faccenna, A. Heuret, S. Lallemand, E. D. Giuseppe, and T. W. Becker (2008), Trench migration, net rotation and slab–mantle coupling, *Earth Planet. Sci. Lett.*, *271*, 233–240.
Gorbatov, A., and Y. Fukao (2005), Tomographic search for missing link between the remnant Farallon slab and present Cocos subduction, *Geophys. J. Int.*, *160*, 849–854.
Grand, S. P. (2002), Shear-wave tomography and the fate of subducted slabs, *Philos. Trans. R. Soc. London A*, *360*, 2475–2481.
Grand, S. P., R. van der Hilst, and S. Widiyantoro (1997), Global seismic tomography: A snapshot of convection in the Earth, *GSA Today*, *7*, 1–7.
Hafkenscheid, E., S. J. H. Buiter, M. J. R. Wortel, W. Spakman, and H. Bijwaard (2001), Modeling the seismic velocity structure beneath Indonesia: A comparison with tomography, *Tectonophysics*, *333*, 35–46.
Hall, R., and W. Spakman (2002), Subducted slabs beneath the eastern Indonesia-Tonga region: Insights from tomography, *Phys. Earth Planet. Inter.*, *201*, 321–336.
Huang, J., and D. Zhao (2006), High-resolution mantle tomography of China and surrounding regions, *J. Geophys. Res.*, *111*, B09305, doi:10.1029/2005JB004066.
Humphreys, E., and R. W. Clayton (1988), Adaptation of back projection tomography to seismic travel time problems, *J. Geophys. Res.*, *93*, 1073–1085.
Ito, E., and H. Sato (1991), Aseismicity in the lower mantle by superplasticity of the descending slab, *Nature*, *351*, 140–141.
Kaneshima, S. (2003), Small-scale heterogeneity at the top of the lower mantle around the Mariana slab, *Earth Planet. Sci. Lett.*, *209*, 85–101.
Kaneshima, S. (2009), Seismic scatterers at the shallowest lower mantle beneath subducted slabs, *Earth Planet. Sci. Lett.*, *286*, 304–315.
Kawakatsu, H., and F. Niu (1994), Seismic evidence for a 920 km discontinuity in the mantle, *Nature*, *371*, 301–305.
Kennett, B. L. N., and A. Gorbatov (2004), Seismic heterogeneity in the mantle-strong shear wave signature of slabs from joint tomography, *Phys. Earth Planet. Inter.*, *146*, 88–100.

Kind, R., and X. Li (2007), Deep earth structure-transition zone and mantle discontinuities, in *Seismology and the Structure of the Earth*, Treatise on Geophysics, vol. 1, edited by B. Romanowicz and A. M. Dziewonski, pp. 591–618, Elsevier, Amsterdam, The Netherlands.

Kubo, T., E. Ohtani, T. Kato, S. Urakawa, A. Suzuki, Y. Kanbe, K. Funakoshi, W. Utsumi, T. Kikegawa, and K. Fujino (2002a), Mechanisms and kinetics of the post-spinel transformation in Mg2SiO4, *Phys. Earth Planet. Inter.*, *129*, 153–171.

Kubo, T., E. Ohtani, T. Kondo, T. Kato, M. Toma, T. Hosoya, A. Sano, T. Kikegawa, and T. Nagase (2002b), Metastable garnet in oceanic crust at the top of the lower mantle, *Nature*, *420*, 803–806.

Li, C., and R. D. van der Hilst (2010), Structure of the upper mantle and transition zone beneath Southeast Asia from traveltime tomography, *J. Geophys. Res.*, *115*, B07308, doi:10.1029/2009JB006882.

Li, C., R. D. van der Hilst, E. R. Engdahl, and S. Burdick (2008), A new global model for *P* wave speed variations in Earth's mantle, *Geochem. Geophys. Geosyst.*, *9*, Q05018, doi:10.1029/2007GC001806.

Martinod, J., L. Husson, P. Roperch, B. Guillaume, and N. Espurt (2010), Horizontal subduction zones, convergence velocity and the building of the Andes, *Earth Planet. Sci. Lett.*, *299*, 299–309.

Mercerat, E. D., and G. Nolet (2013), On the linearity of cross-correlation delay times in finite-frequency tomography, *Geophys. J. Int.*, *192*, 681–687.

Miller, M. S., B. L. N. Kennett, and G. S. Lister (2004), Imaging changes in morphology, geometry, and physical properties of the subducting Pacific plate along the Izu–Bonin–Mariana arc, *Earth Planet. Sci. Lett.*, *224*, 363–370.

Mitrovica, J. X., and A. M. Forte (2004), A new inference of mantle viscosity based upon joint inversion of convection and glacial isostatic adjustment data, *Earth Planet. Sci. Lett.*, *225*, 177–189.

Miyamachi, H., et al. (2009), Construction of the broadband seismic network in Far Eastern Russia for imaging the stagnant slab, *Geophys. Bull. Hokkaido Univ.*, *72*, 37–49 (in Japanese with English abstract).

Morra, G., D. A. Yuen, L. Boschi, P. Chatelain, P. Koumoutsakos, and P. J. Tackley (2010), The fate of the slabs interacting with a density/viscosity hill in the mid-mantle, *Phys. Earth Planet. Inter.*, *180*, 271–282.

Niu, F., and H. Kawakatsu (1995), Direct evidence for the undulation of the 660-km discontinuity beneath Tonga: Comparison of Japan and California array data, *Geophys. Res. Lett.*, *22*, 531–534.

Niu, F., H. Kwakatsu, and Y. Fukao (2003), Seismic evidence for a chemical heterogeneity in the midmantle: A slightly dipping and strong seismic reflector at mid-depth beneath the Mariana subduction zone, *J. Geophys. Res.*, *108*(B9, 2419), doi:10.1029/2002JB002384.

Obayashi, M., D. Suetsugu, and Y. Fukao (2004), PP-P differential traveltime measurement with crustal correction, *Geophys. J. Int.*, *157*, 1152–1162.

Obayashi, M., J. Yoshimitsu, and Y. Fukao (2009), Tearing of stagnant slab, *Science*, *324*, 1173–1175.

Obayashi, M., J. Yoshimitsu, G. Nolet, Y. Fukao, H. Shiobara, H. Sugioka, H. Miyamachi, and Y. Gao (2013), Finite frequency whole mantle P-wave tomography: Improvement of subducted slab images, *Geophys. Res. Lett.*, *40*, 1–6, doi:10.1002/2013GL057401.

Oki, S., Y. Fukao, and M. Obayashi (2004), Reference frequency of teleseismic body waves, *J. Geophys. Res.*, *109*, B04304, doi:10.1029/2003JB002821.

Ren, Y., E. Stutzmann, R. D. van der Hilst, and J. Besse (2007), Understanding seismic heterogeneities in the lower mantle beneath the Americas from seismic tomography and plate tectonic history, *J. Geophys. Res.*, *112*, B01302, doi:10.1029/2005JB004154.

Replumaz, A., H. Kárson, R. van der Hilst, J. Besse, and P. Tapponnier (2004), 4-D evolution of SE Asia's mantle from geological reconstructions and seismic tomography, *Earth Planet. Sci. Lett.*, *221*, 103–115.

Ribe, N. M., E. Stutzmann, Y. Rena, and R. van der Hilst (2007), Buckling instabilities of subducted lithosphere beneath the transition zone, *Earth Planet. Sci. Lett.*, *254*, 173–179.

Richards, S., G. Lister, and B. Kennett (2007), A slab in depth: Three-dimensional geometry and evolution of the Indo-Australian plate, *Geochem. Geophys. Geosyst.*, *8*, Q12003, doi:10.1029/2007GC001657.

Richards, S., R. Holm, and G. Barber (2011), When slabs collide: A tectonic assessment of deep earthquakes in the Tonga-Vanuatu region, *Geology*, *39*, 787–790.

Schellart, W. P., D. R. Stegman, and J. Freeman (2008), Global trench migration velocities and slab migration induced volume fluxes: Constraints to find an Earth reference frame based on minimizing viscous dissipation, *Earth Sci. Rev.*, *88*, 118–144.

Schöffel, H.-J., and D. Das (1999), Fine details of the Wadati-Benioff zone under Indonesia and its geodynamic implications, *J. Geophys. Res.*, *104*, 13,101–13,114.

Shiobara, H., K. Baba, H. Utada, and Y. Fukao (2009), Ocean bottom array probes stagnant slab beneath the Philippine Sea, *Eos Trans. AGU*, *90*(9), 70–71.

Sigloch, K. (2011), Mantle provinces under North America from multifrequency P wave tomography, *Geochem. Geophys. Geosyst.*, *12*, Q02W08, doi:10.1029/2010GC003421.

Sigloch, K., and M. G. Mihalynuk (2013), Intra-oceanic subduction shaped the assembly of Cordilleran North America, *Nature*, *496*, 50–56.

Sigloch, K., N. McQuarrie, and G. Nolet (2008), Two-stage subduction history under North America inferred from multiple-frequency tomography, *Nat. Geosci.*, *1*, 458–462.

Simmons, N. A., S. C. Myers, G. Johannesson, and E. Matzel (2012), LLNL-G3Dv3: Global P wave tomography model for improved regional and teleseismic travel time prediction, *J. Geophys. Res.*, *117*, B10302, doi:10.1029/2012JB009525.

Stegman, D. R., R. Farrington, F. A. Capitanio, and W. P. Schellart (2010), A regime diagram for subduction styles from 3-D numerical models of free subduction, *Tectonophysics*, *483*, 29–45.

Steinberger, B. (2000), Slabs in the lower mantle—Results of dynamic modeling compared with tomographic images and the geoid, *Phys. Earth Planet. Inter.*, *118*, 241–257.

Steinberger, B., and R. Holme (2008), Mantle flow models with core-mantle boundary constraints and chemical heterogeneities in the lowermost mantle, *J. Geophys. Res.*, *113*, B05403, doi:10.1029/2007JB005080.

Torii, Y., and S. Yoshioka (2007), Physical conditions producing slab stagnation: Constraints of the Clapeyron slope, mantle viscosity, trench retreat, and dip angles, *Tectonophysics*, *445*, 200–209.

van der Hilst, R. (1995), Complex morphology of subducted lithosphere in the mantle beneath the Tonga trench, *Nature*, *374*, 154–157.

van der Hilst, R., and T. Seno (1993), Effects of relative plate motion on the deep structure and penetration depth of slabs below the Izu-Bonin and Mariana island arcs, *Earth Planet. Sci. Lett.*, *120*, 375–407.

van der Hilst, R., R. Engdahl, W. Spakman, and G. Nolet (1991), Tomographic imaging of subducted lithosphere below northwest Pacific island arcs, *Nature*, *353*, 37–43.

van der Hilst, R., S. Widiyantoro, and R. Engdahl (1997), Evidence for deep mantle circulation from global tomography, *Nature*, *386*, 578–584.

van der Meer, D. G., W. Spakman, D. J. J. van Hinsbergen, M. L. Amaru, and T. H. Torsvik (2009), Towards absolute plate motions constrained by lower-mantle slab remnants, *Nat. Geosci.*, *3*, 36–40, doi:10.1038/NGEO708.

Wen, L., and D. L. Anderson (1995), The fate of slabs inferred from seismic tomography and 130 million years of suduction, *Earth Planet. Sci. Lett.*, *133*, 185–198.

Wen, L., and D. L. Anderson (1997), Layered mantle convection: A model for geoid and topography, *Earth Planet. Sci. Lett.*, *146*, 367–377.

Widiyantoro, S., and R. van der Hilst (1996), Structure and evolution of subducted lithosphere beneath the Sunda arc, Indonesia, *Science*, *271*, 1566–1570.

Widiyantoro, S., J. D. Pesicek, and C. H. Thurber (2011), Subducting slab structure below the eastern Sunda arc inferred from non-linear seismic tomographic imaging, *Geol. Soc. London Spec. Publ.*, *355*, 139–155.

Yamazaki, D., T. Yoshino, T. Matsuzaki, T. Katsura, and A. Yoneda (2009), Texture of (Mg,Fe)SiO$_3$ perovskite and ferro-periclase aggregate: Implications for rheology of the lower mantle, *Phys. Earth Planet. Inter.*, *174*, 138–144.

Yanagisawa, T., Y. Yamagishi, Y. Hamano, and D. R. Stegman (2010), Mechanism for generating stagnant slabs in 3-D spherical mantle convection models at Earth-like conditions, *Phys. Earth Planet. Inter.*, *183*, 341–352.

Zhao, D. (2004), Global tomographic images of mantle plumes and subducting slabs: Insight into deep Earth dynamics, *Phys. Earth Planet. Inter.*, *146*, 3–34.

Zhao, D., Y. Tian, J. Lei, L. Liu, and S. Zheng (2009), Seismic image and origin of the Changbai intraplate volcano in East Asia: Role of big mantle wedge above the stagnant Pacific slab, *Phys. Earth Planet. Inter.*, *173*, 197–206.

Zhao, D., F. Pirajno, N. L. Dobretsov, and L. Liu (2010), Mantle structure and dynamics under East Russia and adjacent regions, *Russ. Geol. Geophys.*, *51*, 925–938.